Analysis and Extrapolation of D Meson Cross Sections at the LHC

Jeremy Wilkinson
jeremy.wilkinson08@imperial.ac.uk

June 27, 2011

Abstract

The cross sections of D meson production from the ALICE experiment were analysed, using the FONLL and MNR pQCD frameworks as references. The MNR calculations were found to have good agreement with experimental data within MNR's uncertainty band. Experimental data for *pp* collisions was successfully scaled from 7TeV to 2.76TeV to create a reference for lead-lead collisions. Additionally, the cross section of charm production was extrapolated to the full phase space, and the result was found to agree closely with other LHC experiments.

Die Wirkungsquerschnitten zur D-Meson Produktion aus dem ALICE-Experiment wurden im Rahmen von perturbativen QCD Rechnungen mit FONLL und MNR analysiert. Experimentelle Daten aus Proton-Proton-Kollisionen wurden erfolgreich von 7TeV nach 2.76 skaliert, um einen Referenzspektrum für Blei-Blei Kollisionen zu generieren. Zusätzlich wurde der Wirkungsquerschnitt zur Charm-Anticharm Produktion auf den gesamten Phasenraum extrapoliert. Das Ergebnis dieser Extrapolation stimmt mit Ergebnissen aus anderen LHC-Experimenten gut überein. Der experimentelle Wirkungsquerschnitt wird im Rahmen von Rechnungen mit MNR innerhalb der recht großen Unsicherheiten gut beschrieben.

Contents

1 Preface

In this work I have been analysing the cross sections of D meson production provided by the ALICE experiment at the LHC. For most of the analysis, a perturbative QCD calculation framework known as MNR was used. As the rapidity acceptance of the calculations is hard-coded into MNR rather than being set as a free parameter, the source code of the MNR framework was altered and recompiled on the cluster at the Physikalisches Institut at the University of Heidelberg. This allowed the calculation procedure to be modified to suit different experiments. A script was also written to ensure that the program was creating outputs correctly. The calculations were performed for proton-proton collisions at a variety of different collision energies, rapidity acceptances and parameter sets, all of which will be outlined in this report.
All of the analysis of the data was performed using the ROOT analysis framework, which is based on C++ and involves many proprietary classes for the plotting of graphs and histograms. All of the graphs produced for the purposes of this project, and most of the calculations outside the initial pQCD calculations, were performed using this program. Some time was spent at the start of the project learning the ins and outs of this system, meaning that I have gained fluency in the use of this powerful tool through this project.
The ALICE preliminary results for differential cross sections, as well as the FONLL predictions (performed originally by M. Cacciari) and FONLL scaling calculations, were obtained through private communication with Z. Conesa del Valle at CERN and Y. Wang in Heidelberg. All of the scalings using MNR were performed by myself, as well as the rebinning of the scaled predictions for better comparison at 2.76TeV; the rebinning of the experimental data from CDF; and the ratio calculations for determining the reliability of the scalings compared to the CDF data. The result of the interpolation is a D meson reference spectrum at 2.76TeV which will be compared to results from lead-lead collisions.
The extrapolations of the ALICE data also used the preliminary cross sections and the FONLL predictions, and were performed by me using methods suggested by my supervisor, K. Schweda, and A. Dainese, the head of the ALICE Heavy Flavour Working Group (PWG3). The result is an estimate of the total charm production cross section at LHC energies (both 2.76TeV and 7TeV), which was seen to be in agreement with the results of two other experiments (LHCb and ATLAS), as well as the theoretical trend from next-to-leading-order calculations.
Throughout the project, feedback and suggestions were received from the rest of the Heavy Flavour Working Group during their regular paper preparation (D2H) meetings which were held over conference call, where I presented and received comments on my findings for both the reference spectrum calculations and the extrapolations of the cross section data. This culminated in May in the extrapolations being reported to the ALICE Physics Forum, and my results being accepted as the ALICE preliminary findings, which have already been presented at two recent international conferences.

2 Introduction

2.1 Motivation

One of the leading experiments taking place at the LHC is the study of the quark-gluon plasma (or QGP), an aggregate state of matter in which quarks and gluons are not confined into hadrons. This only occurs at exceedingly high temperatures or pressures, for example in conditions similar to those shortly after the Big Bang. Similar conditions can be recreated in heavy ion experiments, where large nuclei are collided against one another at high energies, for example at the Relativistic Heavy Ion Collider (RHIC) or the Large Hadron Collider. The ALICE experiment[1] is the dedicated experiment for studies into the QGP using these heavy ion collisions.
Quarkonium production – the production of flavourless mesons consisting of a heavy quark and its antiquark – at the LHC is an important signature of QGP formation.[2] Two species of quarkonium exist: charmonium ($c\bar{c}$) and bottomonium ($b\bar{b}$). Toponium ($t\bar{t}$) does not exist as the lifetime of the top quark is too short for hadronisation to occur.

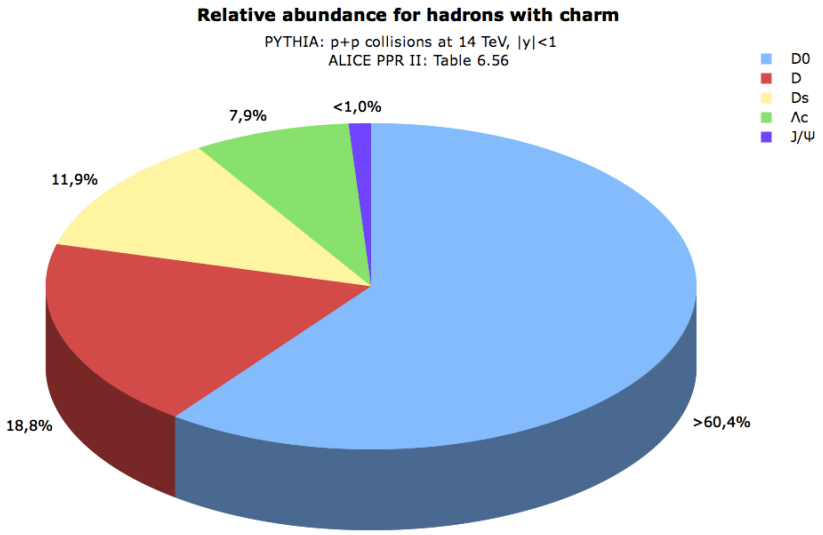

Figure 2.1: Relative probabilities of $c \to H$.

The first radial excitation of charmonium is the J/ψ particle. This particle carries about one percent of all the charm quarks produced in collisions, as seen in figure 2.1.

The total charm cross section is a vital ingredient for statistical model calculations, and can be measured by experiment. As we see from figure 2.1, most of the charm produced in collisions is carried by D mesons. Hence, these provide a very large statistical background for the analysis of charm production. The measurement of D meson production is therefore incredibly useful for the statistical model calculations on the production of charmonium, allowing us to better study the properties of the QGP.

2.2 Introduction to the LHC experiment

The Large Hadron Collider, or LHC, is a particle collider at the European Organisation for Nuclear Research (CERN) based near Geneva. It is the highest-energy and highest-luminosity particle collider in the world, providing recently a record collision energy of $\sqrt{s} = 7\text{TeV}$ and a peak luminosity of $L = 3.4 \times 10^{32}\text{cm}^{-2}\text{s}^{-1}$. It recently exceeded an integrated luminosity of 1000 inverse picobarns for the year's analysis, after only a couple of months of collisions. The collider ring is 27km in circumference, and when fully operational it is designed to provide proton-proton collisions at a center-of-mass energy $\sqrt{s} = 14\text{TeV}$, and lead-lead collisions at $\sqrt{s_{NN}} = 5.5\text{TeV}$.

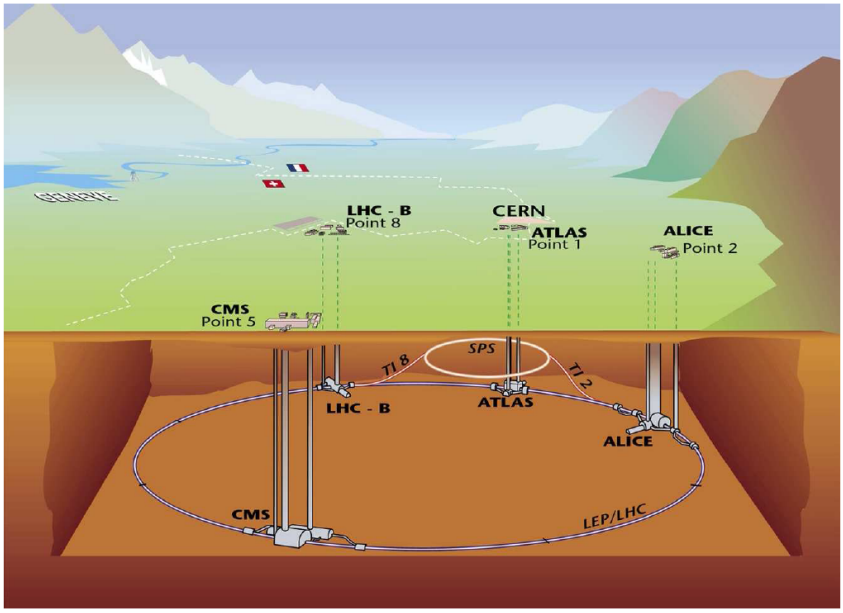

Figure 2.2: A schematic sketch of the Large Hadron Collider, highlighting the positions of the four main detectors.[3]

There are four main detectors at the LHC – three of which mainly study proton-proton

collisions (ATLAS, CMS, and LHCb), and one which will mainly benefit from lead-lead collisions (ALICE). The layout of the LHC is shown in figure 2.2, which displays the interaction points – the positions in the ring where the two particle tubes intersect and collisions are carried out.

- **ATLAS** (**A** **T**oroidal **L**HC **A**pparatus), aims primarily to detect the Higgs Boson, as well as searching for evidence of physics beyond the standard model, for example extra dimensions and supersymmetric particles.
- **CMS** (the **C**ompact **M**uon **S**olenoid) has the same overall goal as ATLAS, approaching its measurements using alternative detector technologies.
- **LHCb** (**LHC b**eauty) aims to observe charge-parity violation in systems involving B mesons, helping to explain the apparent asymmetry of matter and antimatter in the universe.
- **ALICE**[1] (**A** **L**arge **I**on **C**ollider **E**xperiment) is dedicated to heavy ion collisions. Its main goal is to identify and characterise the quark-gluon plasma, a deconfined phase of matter where quarks are free of their usual hadronic boundaries.

The ALICE detector is composed of various subdetectors, for example:

- **Time of Flight** – measures the time of flight of particles from the interaction point. This information is used to identify particles.
- **Time Projection Chamber** – reconstructs particle tracks via the charge deposited in a cloud of neon and carbon dioxide.
- **Inner Tracking System** – provides high spatial resolution and secondary vertexing capabilities.
- **Transition Radiation Detector** – analyses the mass of particles based on the amount of radiation given off when they decelerate.

3 Theoretical Background

3.1 The MNR calculation framework

MNR is a next-to-leading-order perturbative QCD calculation framework devised by Mangano, Nason and Ridolfi in 1992[4,5] to calculate the cross sections of heavy quark production in strong interactions. The production of charmed hadrons in pp collisions can be calculated in pQCD according to equation 3.1:

$$d\sigma(pp \to D+X) = \sum_{i,j,k} \int dx_1 dx_2 dz f_i(x_1,\mu_f) f_j(x_2,\mu_f) \times d\sigma_{ij\to kX}(\mu_F,\alpha_S(\mu_R),m_c) D_k^D(z), \tag{3.1}$$

where i and j indicate the interacting partons (gluons or quarks) in the colliding protons, carrying a fraction of the proton's momentum x; f_i is the structure function; α_s is the strong coupling constant; D_k^D is the fragmentation function describing the probability of the outgoing heavy quark k (for example, charm) fragmenting to a D meson, which will be further discussed in section 3.2; m_c is the mass of the charm quark; μ_F and μ_R are the factorisation and renormalisation scales, and finally the cross section $d\sigma$ is the hard scattering cross section which is calculated in pQCD.

The structure function is also known as the parton distribution function, which describes the probability of the parton i having momentum fraction x within the colliding proton. This cannot be determined via perturbative means, so these are obtained through experimental data instead. The PDF which was used for the MNR calculations was CTEQ6m.[6]

There are three leading processes in the LHC which produce heavy quarks; these are pair production, gluon splitting, and flavour excitation. The Feynman diagrams for these processes are shown in figures 3.1, 3.2 and 3.3.

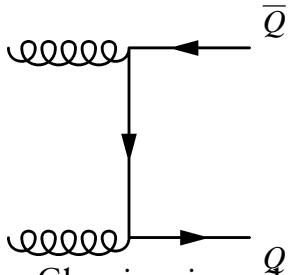

Figure 3.1: Gluonic pair production.

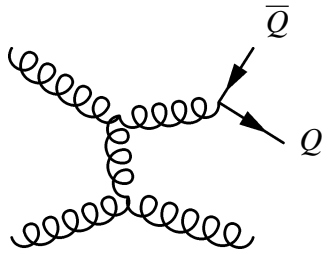

Figure 3.2: Gluon splitting.

Pair production is a hard process whereby two gluons, or a quark-antiquark pair, are annihilated and form a $c\bar{c}$ pair in the final state. Gluon splitting is a next-to-leading-order process involving the hard scattering of two gluons, resulting in an outgoing quark-antiquark pair and one gluon in the final state. Finally, flavour excitation is where a gluon from one proton splits into a $c\bar{c}$ pair, which is then hard scattered by a gluon from the other proton.

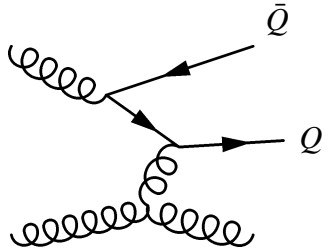

Figure 3.3: Flavour excitation.

As quarks do not exist alone, and are only seen bound into hadrons (either as a meson when paired with an antiquark or as a baryon when grouped with two other quarks), their mass is not a well-defined quantity, and is scale dependent. This scale dependence is consequent to the bare quark being surrounded by gluons and quark-antiquark pairs.[7] The energy of the cloud bound within a sphere around the quark increases with radius, and as a result of this so does its effective mass. Within this thesis an explicit scale dependence of the quark mass is not considered, but the mass is instead varied between 1.3 and 1.7 GeV/c^2 for charm quarks and between 4.5 and 5.0 GeV/c^2 for bottom quarks.

The MNR framework only includes leading- and next-to-leading-order terms and neglects all higher orders. The effects of the higher orders are absorbed by the renormalisation scale μ_R. A complete calculation would be independent of the chosen value of the scale, however such a perfected calculation is not possible due to singularities

caused by short-distance (ultraviolet) divergences. μ_R is taken in units of μ_0,[8] with

$$\mu_0 = \sqrt{m_Q^2 + 0.5 \times (p_t^2(Q) + p_t^2(\bar{Q}))} \approx m_t, \tag{3.2}$$

where $m_t = \sqrt{m_Q^2 + p_T^2}$. The central value for μ_R is taken to be equal to μ_0, and is varied between $0.5\mu_0$ and $2.0\mu_0$ in order to estimate the uncertainty caused by the choice of μ_R.

There is a second scale to take care of singularities arising due to long-distance (infrared) divergences, known as the factorisation scale.[9] Again, this scale alone has no particular physical meaning, and an ideal framework would have no dependence on this. This is also taken in units of μ_0, and is also varied between $0.5\mu_0$ and $2.0\mu_0$, with a central value of μ_0. An additional constraint is placed on the scales in order to reduce overall uncertainties, namely that they cannot be more than a factor of two apart. Thus, the constraints on the scales are as follows:

$$0.5 \leq \frac{\mu_F}{\mu_0}, \frac{\mu_R}{\mu_0}, \frac{\mu_F}{\mu_R} \leq 2.0 \tag{3.3}$$

The differential cross section spectra are calculated with respect to the transversal momentum of produced particles p_T – their momentum component transverse to the beam direction – and their rapidity y. Rapidity is a measure of how much of the particle's momentum lies in the direction of the beam axis, and is defined in equation 3.4:

$$y = \frac{1}{2} \ln \frac{E + p_z c}{E - p_z c}, \tag{3.4}$$

where E is the total energy of the particle, p_z is the component of the particle's momentum in the direction of the beam axis, and c is the speed of light. The program used calculates p_T spectra for both the full rapidity range and for rapidity up to a certain cutoff, allowing a calculated p_T spectrum to better match with experimental acceptances. Originally this was defined to be $|y| \leq 1$ in the calculation package used, however the source code was altered within this thesis and the program recompiled to allow for calculations with alternative rapidity cutoffs.

3.2 Fragmentation

Due to colour neutrality – the postulate in quantum chromodynamics that results in colour-charged particles being unable to exist alone – the heavy quarks produced in particle collisions hadronise soon after production. This process is also known as fragmentation. The leading cause for this occurrence stems from the nature of the strong

force. In contrast to the other two fundamental forces of the Standard Model (weak and electromagnetic), the effect of the strong force between two quarks does not reduce with increasing distance – in fact, it increases linearly with relative distance at large separations, as if the two quarks were bound together by a spring. This means that once the two quarks are a long enough distance from each other, the energy between them is such that it is more energetically favourable for a quark-antiquark pair to be produced from the vacuum rather than for the original quark-antiquark pair to remain bound to each other at such a separation.

As hadronisation is a soft process, it is not possible to describe it in perturbative QCD calculations. Instead it must be modelled by experimentally-determined fragmentation functions. C. Peterson *et al.*[10] devised such a fragmentation function from simple quantum mechanical considerations in 1983, which is dependent on the energy of the hadron compared with the energy of the incident quark:

$$D_Q^H(z) \propto \frac{1}{z[1-(1/z)-\varepsilon_Q/(1-z)]^2}, \tag{3.5}$$

where $z = E_H/E_Q$, E_Q is the energy of the incoming heavy quark, and E_H is the energy of the outgoing hadron. The parameter ε_Q in this equation is technically defined as $\varepsilon_Q = (m_q/m_Q)^2$, but for calculation purposes it is taken to be a free parameter. The function described in equation 3.5 is displayed in figure 3.4 for the fragmentation of bottom and charm quarks, with $\varepsilon_b = 0.006$ and $\varepsilon_c = 0.06$. These are commonly-used values for these quark species.[11]

The peak of the fragmentation function is the relative energy at which the largest proportion of fragmentations occur. This occurs at $z \approx 1 - \sqrt{\varepsilon_Q}$. The difference in the ε_Q values for the two quark species is easily explainable kinematically – as bottom quarks are heavier than charm quarks, the resulting hadrons will have their momentum reduced far less as a result of combining with the slower light quarks, thus b-flavoured hadrons will have, on average, a higher relative energy than c-flavoured hadrons. The overall effect of this is that the differential cross section spectra are "smeared out", so to speak, with this effect being far more significant for charm than beauty. This has been measured at LEP at the Z resonance,[12] with the peak occurring at relative momentum fraction $\langle x \rangle = 0.484 \pm 0.008$ for charm and $\langle x \rangle = 0.702 \pm 0.008$ for beauty. The MNR framework includes Peterson fragmentation as a part of the calculations. Due to the masses of heavy quarks not being physically well-defined (as discussed in section 3.1), ε_Q is left as a free parameter in the framework. It is defined in the calculation program at the same time as the quark mass and the factorisation and renormalisation scales. For the purposes of finding uncertainties on the calculations caused by the change in ε_Q, this parameter was altered whilst using central values for mass and scales.

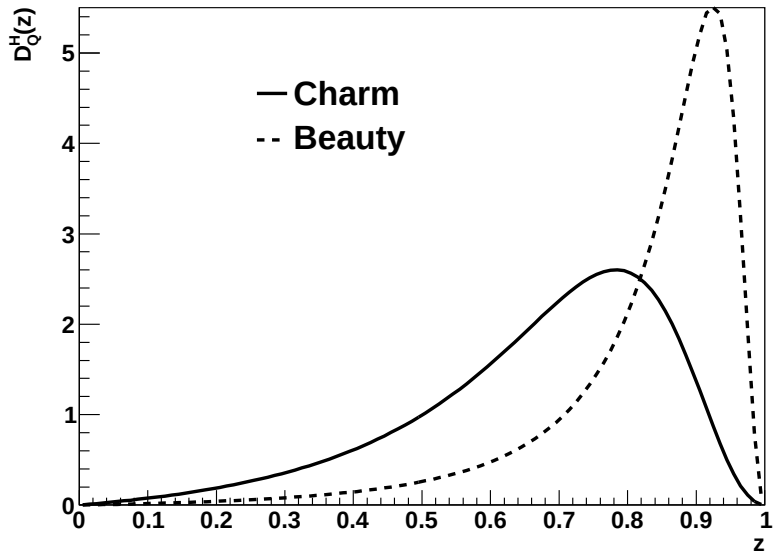

Figure 3.4: The fragmentation function of c and b with respect to the hadron energy z. ε_c is taken to be 0.06, and ε_b is equal to 0.006. Both curves are normalised to unity.

Other commonly-used fragmentation functions include the Kartvelishvili-Likhoded-Petrov function,[13] the Bowler function[14] and the Collins-Spiller function,[15] all of which also have parameters which must be fitted to experimental data.

3.3 Spectra and central parameters

The results of the MNR calculations are shown in figures 3.5 and 3.6, which display the p_T and rapidity spectra for charm production at 7TeV, with the different lines representing alternative combinations for the scaling parameters. It can be seen from these that the vast majority of the cross section is accounted for within the region $p_T \leq 20$GeV/c and $|y| \leq 6$. We also see that the uncertainties due to the variation of the scales is large, and is at its smallest when μ_F and μ_R are equal to one another. Additionally, the uncertainty is higher at low p_T than at high p_T, with the differences beyond $p_T = 30$GeV/c being largely due to statistical fluctuations, as there are very few particles simulated which have such high transversal momentum.

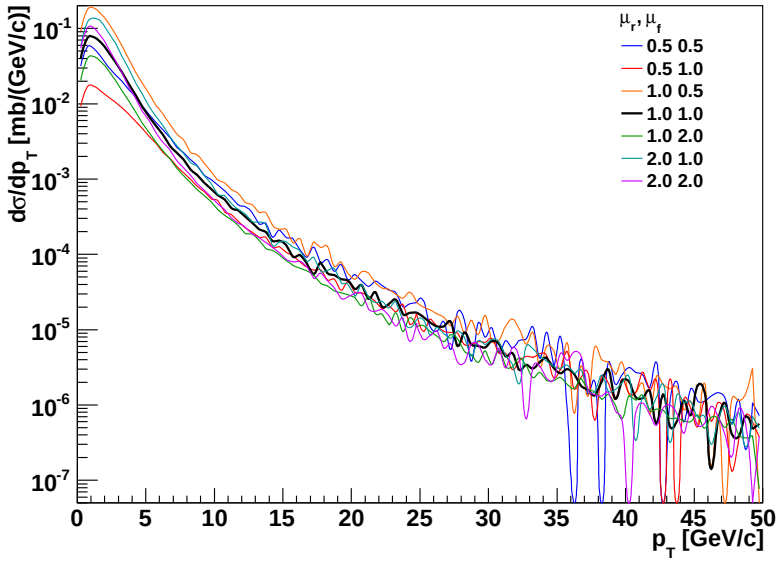

Figure 3.5: The MNR spectrum with respect to $p_T(Q)$.

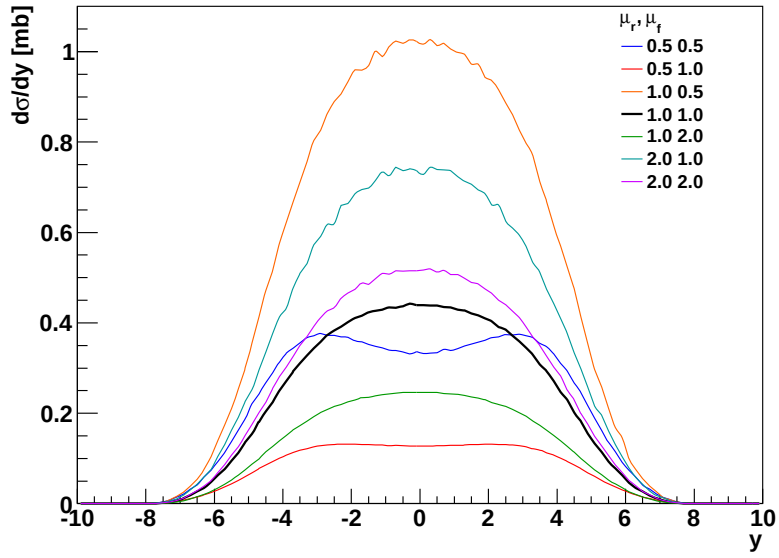

Figure 3.6: The rapidity spectrum from the MNR calculations for charm at 7TeV.

The parameters which were used are outlined in table 3.1, with the bold values being the central parameters.

PDF	**10050** (CTEQ6m)
$m_c/(\mathrm{GeV/c^2})$	1.2, 1.3, 1.4, **1.5**, 1.6, 1.7, 1.8
$m_b/(\mathrm{GeV/c^2})$	4.5, 4.6, 4.7, **4.8**, 4.9, 5.0
μ_F/μ_0	0.5, **1.0**, 2.0
μ_R/μ_0	0.5, **1.0**, 2.0
ε_c	0.002, **0.02**, 0.11
ε_b	0.001, **0.002**, 0.02

Table 3.1: Parameters used for the MNR calculations. The PDF number is the reference for CTEQ6m in the LHAPDF package.[16]

The calculations were run on the cluster at the Physikalisches Institut at Ruprecht-Karls Universität Heidelberg. Typically a run with one parameter set took just over 24 hours, with the cluster allowing 30 such calculations to take place simultaneously. This made it possible to calculate large amounts of data at once with relatively little waiting time. A script was also written to double-check that all the parameter sets were giving output so that any which had not completed successfully could be resubmitted, as there was the possibility that a small percentage of outputs could either not be created or not be returned from the cluster correctly.

3.4 FONLL

FONLL is an alternative approach to perturbative QCD calculations.[8] FONLL stands for Fixed Order plus Next Leading Logarithm. It is a framework which has initial conditions accurate to NLO calculations such as MNR, but has a spectral evolution accurate to the next leading logarithm, allowing there to be less uncertainty at higher p_T. Its relation to first-order calculations is shown in equation 3.6.

$$\sigma_Q^{\mathrm{FONLL}}(p_T, m) = \mathrm{FO} + (\mathrm{RS} - \mathrm{FOM0})G(m, p_T) \tag{3.6}$$

where FO denotes the cross section from NLO calculations, FOM0 is the limit for NLO as m and p_T tend to 0, and RS is the resummed calculation at the limit of $m = 0$. The subtraction here removes any terms which are common between the RS and FO calculations. $G(m, p_T)$ is a suppression factor, defined in equation 3.7.

$$G(m, p_T) = \frac{p_T^2}{p_T^2 + c^2 m^2}, \text{where } c = 5 \tag{3.7}$$

This suppression factor is used as it was observed[17] that at $p_T < 5m$, the massless limit gives unreliable results, so its contribution has to be suppressed. However, this suppression factor does not diminish the NLO+NLL accuracy, as it only affects terms beyond the scope of perturbation theory.
As we see in figure 3.7, there is very little difference between the FONLL spectrum and the MNR spectrum at low p_T, with the only major difference being a smaller uncertainty on FONLL for p_T greater than 3GeV/c, and far less statistical fluctuation at higher p_T. Overall then, we can conclude that by construction FONLL is identical to the MNR framework at low p_T and offers better accuracy at higher transversal momentum. Additionally, the FONLL calculations differ for different species of meson being analysed, whereas MNR assumes the shape of the spectrum to be the same for all mesons fragmented from a particular quark flavour (in the case of charm, this is D^{*+}).

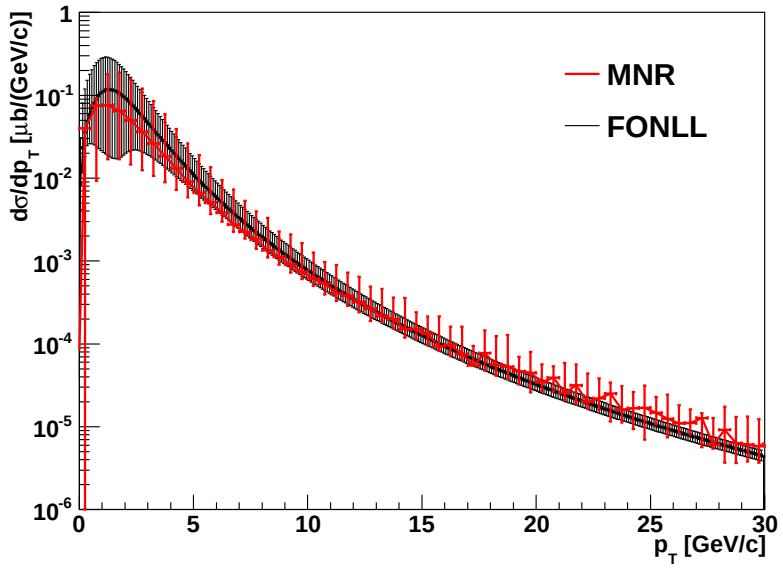

Figure 3.7: A comparison of MNR against FONLL. Error bars are the overall uncertainty caused by the alteration of the scaling variables.

In the end the MNR calculations were performed by me in preference to FONLL as the structure of the program makes it very flexible, easily allowing the alteration of all parameters. This included variables such as the rapidity cutoff used in the calculation of the p_T spectrum, which is a quantity normally hard coded into the program and not a free parameter. The FONLL framework, by comparison, is nowhere near as

easily accessible, and so calculations for this by theoreticians are usually relied upon. The raw FONLL calculations used in this project were performed by M. Cacciari and obtained through private communication.

3.5 Meson species and decay channels

At the ALICE experiment there are three species of charmed meson for which preliminary results have already been measured - these are D^0, D^+ and D^{*+}. These all consist of a c quark and a light antiquark – $\bar{u}$ in the case of D^0 and $\bar{d}$ for D^+ and D^{*+}. The fragmentation ratio represents the relative probability of a charm quark fragmenting into a specific hadron species. These fragmentation ratios have been measured at LEP at the Z-resonance,[18,19] as represented in the introduction in figure 2.1.
The most recent values for the fragmentation ratios from charm admixture are given by the Review of Particle Physics 2010,[20] and are displayed in equation 3.8.

$$\begin{aligned} \mathscr{B}(c \to D^0) &= 0.557 \pm 0.023 \\ \mathscr{B}(c \to D^+) &= 0.226 \pm 0.010 \\ \mathscr{B}(c \to D^{*+}) &= 0.238 \pm 0.007 \end{aligned} \tag{3.8}$$

However, due to their short lifetimes we do not detect these mesons directly - rather, we detect their decay products. These are displayed in equation 3.9.

$$\begin{aligned} D^0 &\to K^- + \pi^+, \\ D^+ &\to K^- + \pi^+ + \pi^+, \\ D^{*+} &\to D^0 + \pi^+ \end{aligned} \tag{3.9}$$

As charm is not conserved in the decays of D^0 and D^+, these must be weak processes, as strong and electromagnetic interactions conserve flavour. The decay of D^{*+}, on the other hand, is a strong decay of the resonance. Figures 3.8 and 3.9 and show possible Feynman diagrams for the decay processes of D^0 and D^+, along with their branching ratios from the Particle Data Group.[20]
The branching ratio of D^{*+} is $\mathscr{B}(D^{*+} \to D^0\pi^+) = 67.7 \pm 0.5\%$. The D^0 created by D^{*+} decay then decays by the process in figure 3.8, leading to an overall branching ratio of $\mathscr{B}(D^{*+} \to K^-\pi^+\pi^+) = (2.63 \pm 5.33 \times 10^{-2})\%$.

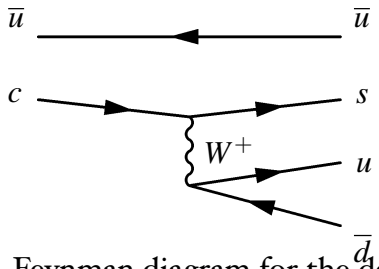

Figure 3.8: Feynman diagram for the decay of D^0.
$\mathscr{B}(D^0 \to K^-\pi^+) = 3.89 \pm 0.05\%$.[20]

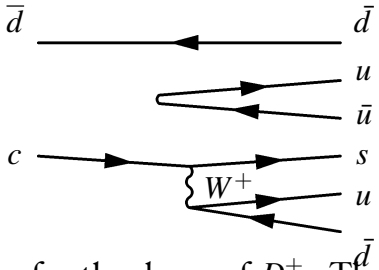

Figure 3.9: Feynman diagram for the decay of D^+. The $u\bar{u}$ pair is created from the vacuum and hadronises with the $\bar{d}$ and s quarks produced by the interaction.
$\mathscr{B}(D^+ \to K^-\pi^+\pi^+) = 9.4 \pm 0.4\%$.[20]

3.6 Correction of feeddown from B

In the experiment, B mesons (mesons containing a bottom quark and a light antiquark) are created as well as D mesons. These decay primarily to D mesons, by processes similar to those mentioned in section 3.5. This complicates the matter of extracting the charm cross section, as the extra D yield from this beauty "feeddown" has no correlation with the charm quarks created directly by the collisions. This means that every measurement we make must be corrected to account for this, so that we can better tell what proportion of detected mesons originated from charm-anticharm pairs.
This is done using pQCD calculations. The spectrum for B meson production is calculated using pQCD framework, in much the same way as for D meson production. This spectrum is then subtracted from the experimental result. Shown in figures 3.10 and 3.11 are plots comparing results from the CMS experiment[21] for B^+ to MNR, as well as the results from two other pQCD approaches: PYTHIA[22] and MC@NLO[23] (**M**onte **C**arlo @ **N**ext-to-**L**eading **O**rder). To produce this spectrum, the MNR spectrum for overall beauty production was scaled by the branching ratio $\mathscr{B}(b \to B^+) = (40 \pm 1)\%$.[20]

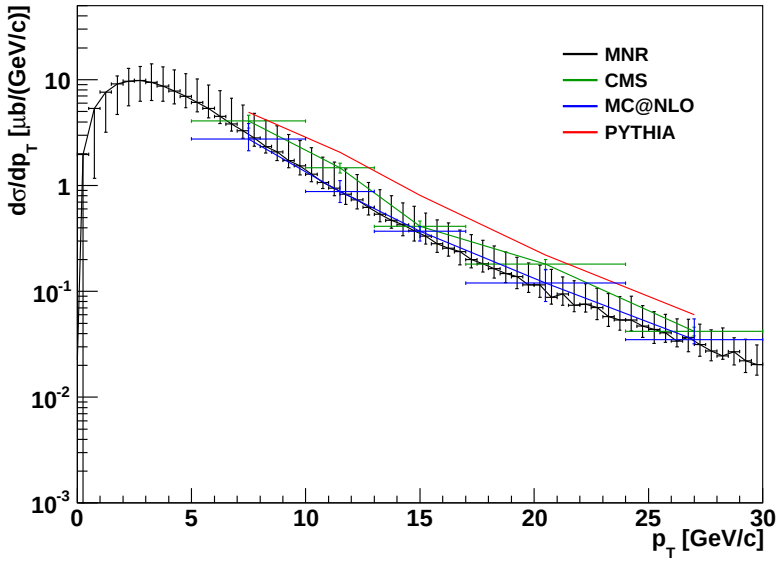

Figure 3.10: Comparison between MNR p_T spectrum for beauty against CMS results.

The uncertainties on the MNR curves are those caused by the alteration of the scaling parameters. The beauty mass m_b used by all of the theoretical calculations in this plot was 4.8GeV/c^2, and the MNR calculations for the p_T spectrum were redefined to have a rapidity cutoff of $|y| < 2.4$ to match the acceptance of the CMS measurements. Here, we see that there is a strong agreement between the MNR calculations and the other frameworks quoted by CMS, especially for MC@NLO (another next-to-leading-order framework) in the p_T spectrum. We see also that there is very strong agreement with the CMS results themselves. The preliminary spectra used in the analysis in this project have already been corrected for feeddown using FONLL, and are shown in figures 3.12, 3.13 and 3.14.

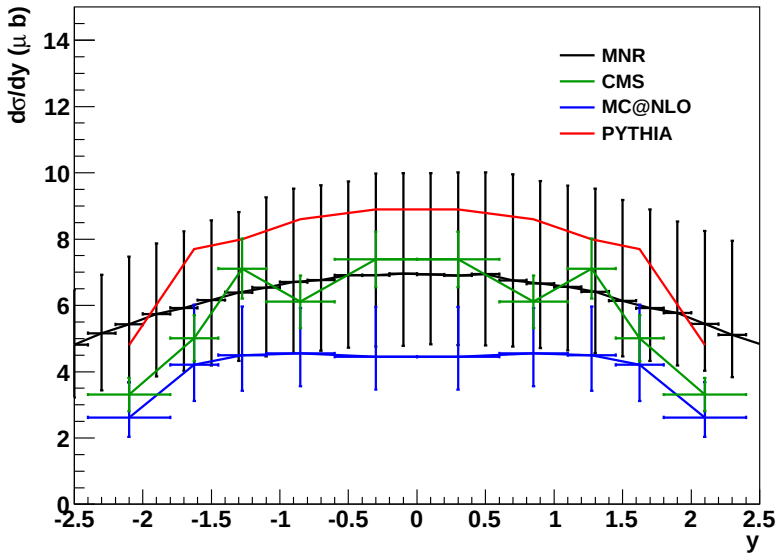

Figure 3.11: Comparison between MNR rapidity spectrum for beauty against CMS results.

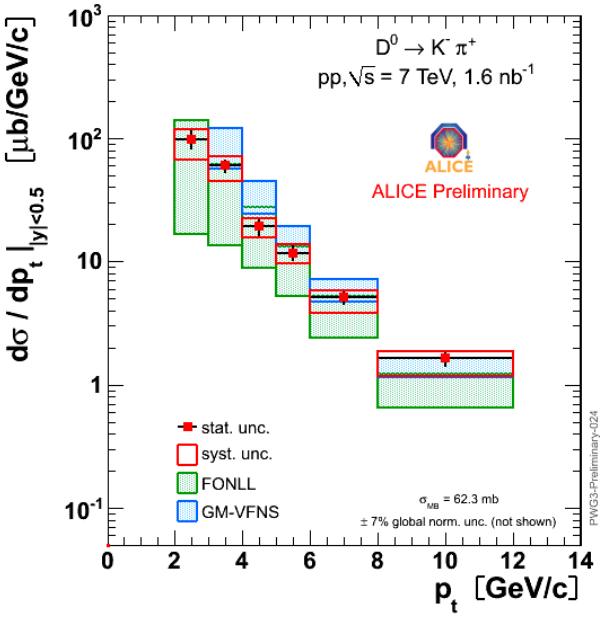

Figure 3.12: The feeddown-corrected D^0 spectrum for pp at $\sqrt{s} = 7$TeV.

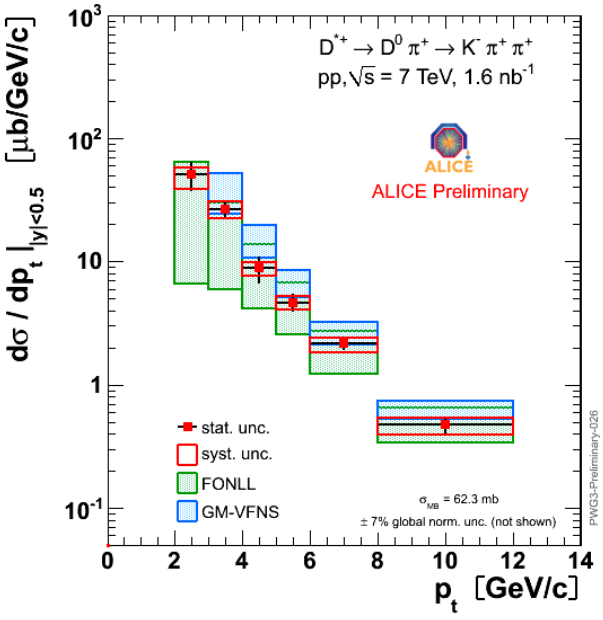

Figure 3.13: The feeddown-corrected D^{*+} spectrum for pp at $\sqrt{s} = 7$TeV.

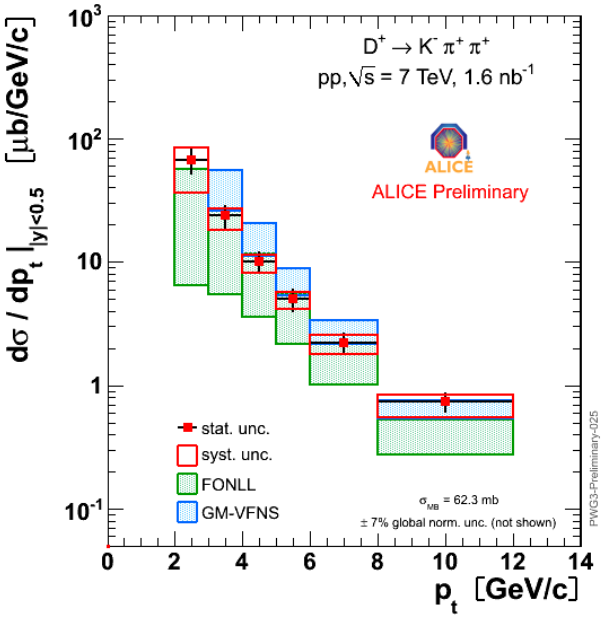

Figure 3.14: The feeddown-corrected D^+ spectrum for pp at $\sqrt{s} = 7$TeV.

4 Energy interpolation

Whilst most of the data from pp collisions is taken at a collision energy of 7TeV, collisions of lead nuclei took place at 2.76TeV. This is because of the magnetic fields used to keep the circulating beams in orbit around the collider, as the strength of the magnetic field is fixed due to the 1232 dipole magnets around the LHC ring. Currently they are operated at the highest available field, which is half of the LHC's full design specification. Due to the Lorentz force, shown in equation 4.1, if the charge-mass ratio is reduced (as is the case when comparing a lead nucleus with a single proton), the momentum must be reduced in order to keep the radius of orbit constant. As the radius of orbit is constrained by the size of the beam tunnel, if this were not done then the beam would be lost to the sides of the tunnel.

$$\mathbf{F} = Q(\mathbf{E} + \mathbf{v} \times \mathbf{B}) \tag{4.1}$$

Proton-proton colisions serve as an important reference to which the lead-lead collisions can be compared. In order to compare results from both energies to each other fully, the experimental data from the proton-proton collisions must be scaled down to 2.76TeV. This is done using results from perturbative QCD calculations at each energy. As a preliminary test, calculations for 1.96TeV with a rapidity cutoff of $|y| \leq 1$ to match CDF acceptance were made, allowing us to scale the proton-proton data to Tevatron energies in order to compare scaled data to already-published data from the CDF collaboration.[24] Once it was determined from this test that the method was reliable, the 2.76TeV reference was then constructed.
Recently, an additional short run was completed over three days for proton-proton collisions at 2.76TeV, so we are able to make a cross check between our reference data and the experimental results.

4.1 Method

To interpolate between two energies, one requires theoretical p_T spectra from the two energies which are to be interpolated between. Once these theoretical spectra have been obtained, a ratio is taken between the two at each p_T bin of the experimental data. This is shown in equation 4.2, where E_2 and y_{cut} define the collision energy and rapidity cutoff at the second energy.

$$\text{Ratio}(p_T) = \frac{\frac{d\sigma(p_T)}{dp_T}(E_2, y \leq y_{cut})}{\frac{d\sigma(p_T)}{dp_T}(7\text{TeV}, |y| \leq 0.5)} \tag{4.2}$$

This is achieved by making simulations for the cross sections which would be achieved at these energies, using the MNR framework discussed in section 3.1. Once the theoretical differential cross sections are obtained, a ratio is taken of the two at each individual momentum range, by which the data from ALICE in each bin is then scaled. As we are interpolating to lower energies, the scaling factor is less than unity in each case. The published CDF data can be rebinned to use the same momentum ranges as the ALICE data by taking weighted averages over the necessary ranges. Once this has been done, the two graphs are plotted side-by-side for direct comparison.

4.2 Uncertainties in the interpolation ratio

As discussed in section 3.1, the pQCD calculations use varying parameters to give an idea of the uncertainties involved in the spectra. The effect on the scaling ratio due to the alteration of these parameters will be discussed in this section. So that rapidity scaling effects, and the uncertainties caused by this, did not have to be considered simultaneously with the variation of parameters (which would have caused possible skewing of the uncertainties), the interpolation ratios between 7TeV and 2.76TeV were used when testing the effect of charm mass, scales, and ε_p.

4.2.1 Dependence on p_T

As the p_T spectra have different shapes at different energies, the ratio between the curves is highly dependent on p_T. Hence it is important to take ratios at each bin, rather than for example attempting to look at the integral over all p_T. The result of this is a comparison which much more accurately takes into account the theoretical differences at each energy level. Due to this I shall also be considering the full p_T spectra when looking at the uncertainties caused by each parameter.

4.2.2 Mass of charm quark

The interpolation ratio was taken between 2.76TeV and 7TeV for each mass value (see table 3.1) separately with central values used for all other parameters, and the results from the three masses were then compared to one another. The uncertainty caused by this is displayed in figure 4.1.
As can be seen, the variation of charm mass has only a very small effect on the interpolation ratio between the two energies, with all three curves almost completely overlapping throughout the entire p_T spectrum. At 2GeV/c this uncertainty is $\pm 3\%$ and for 10GeV/c it is $^{+4}_{-2}\%$.

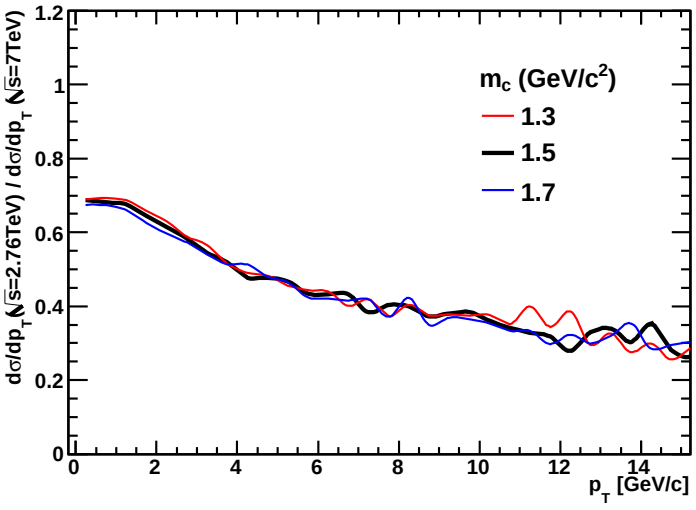

Figure 4.1: The dependence of interpolation ratio on charm quark mass. ε_c, μ_F and μ_R take their central values here.

4.2.3 Peterson fragmentation parameter, ε_P

The Peterson parameter in the QCD calculations was also varied (see table 3.1). Similarly to the procedure with mass, the ε_P values were considered like-for-like when taking the ratios between the spectra, and the result of this comparison is seen in figure 4.2.

As with the mass variation, we see here that there is little effect caused by the variation of ε_P, here $^{+4}_{-7}\%$ at $p_T = 2$ and $^{+10}_{-13}\%$ at 10GeV/c. There is a greater uncertainty of about 40% between 16 and 18 GeV/c, however this seems to be simply due to statistical fluctuations in the calculations, which occur often at higher transversal momenta as previously seen.

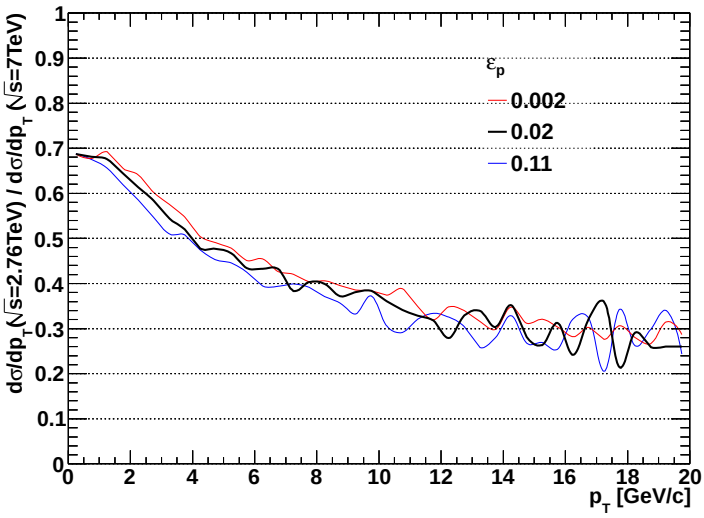

Figure 4.2: The dependence of interpolation ratio on ε_P. m_c, μ_F and μ_R are at central value for all cases.

4.2.4 Scaling parameters, μ_F and μ_R

The scaling parameters of the MNR calculations were both varied as outlined in table 3.1. The variation over all scale sets is presented in figure 4.3.
As can be seen, the uncertainty caused by the scaling variables is far larger than that caused by altering the charm mass or fragmentation parameter. This is more significant as well as it has a far greater effect on the lower p_T end of the spectrum, where the differentials are far larger. As the effect is so large, it is useful to see what this uncertainty is as a percentage of the central parameters. To do this, the lower and upper bounds of the uncertainty are taken over the full spectrum, and then these are divided by the central spectrum. The result of this is displayed in figure 4.4.
The uncertainty caused by the scales are far greater than charm mass or ε, with a $^{+50}_{-10}\%$ error at 2GeV/c, and $\pm 10\%$ error at 10GeV/c. It is concluded from this that the scales are the greatest source of uncertainty in the interpolations by a large margin, as high as 70% at low p_T, and remains high throughout the spectrum. Due to this I will be using the scales as the main source of uncertainty in the calculation of the scaling ratio.

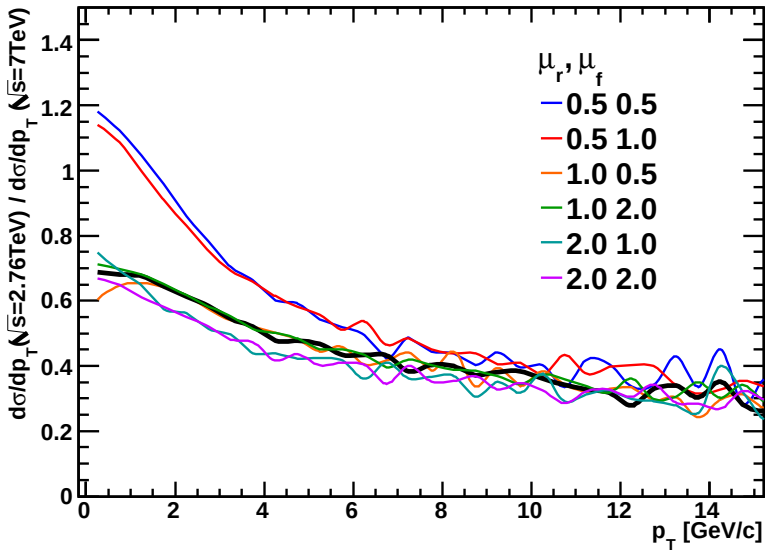

Figure 4.3: The dependence of interpolation ratio on μ_F and μ_R. m_c and ε_c have been kept at their central values.

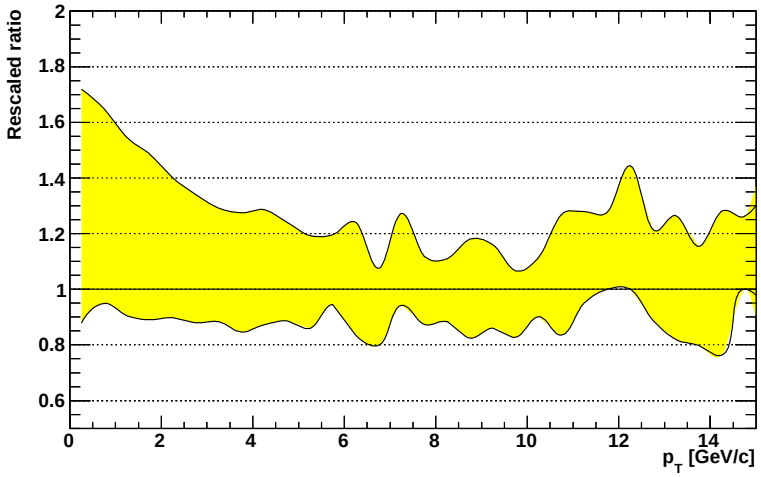

Figure 4.4: The uncertainties caused by the scaling variables as a fraction of the central calculation.

4.3 Interpolation to CDF energy

Data for D meson production from the CDF experiment at Fermilab[24] will act as a test of the method, to see how well the interpolation can be used to create a reference spectrum. If the ALICE data interpolated to CDF energy matches with the data already taken from CDF, then this confirms that this is a valid method to make predictions at other collision energies, and so can be used to create a reference spectrum for 2.76TeV.

4.3.1 Rebinning of CDF data

The first stage is to rebin the CDF data, allowing a direct comparison to be made between the two spectra. As we are dealing with spectra of differential cross section, the rebinning is simply done by taking averages of the CDF data within the ALICE ranges, weighted by the bin widths. The tables in Appendix A contain the published CDF measurements[24] for differential meson cross sections, and the data rebinned to the ALICE p_T bins. Figures 4.5, 4.6 and 4.7 display the rebinning process for D^0, D^+ and D^{*+}, respectively.

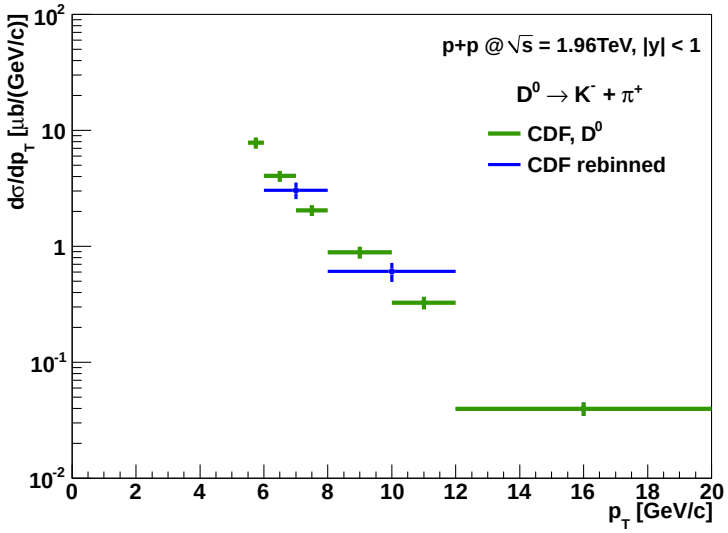

Figure 4.5: Rebinning of D^0 CDF data to ALICE bins.

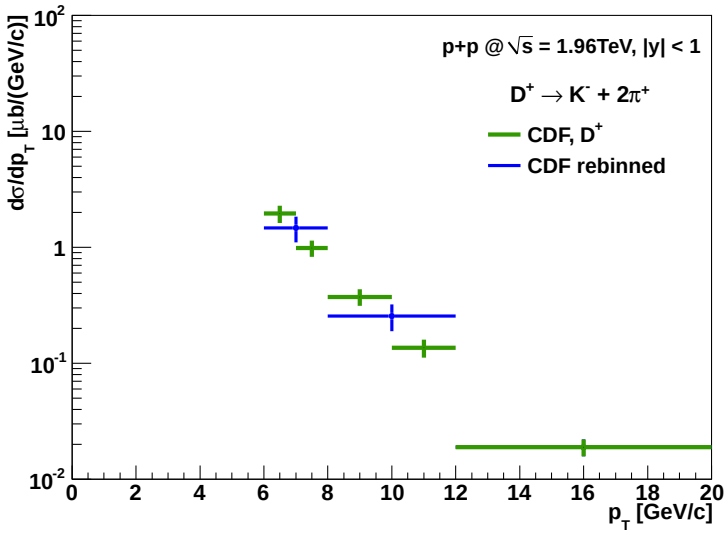

Figure 4.6: Rebinning of D^+ CDF data to ALICE bins.

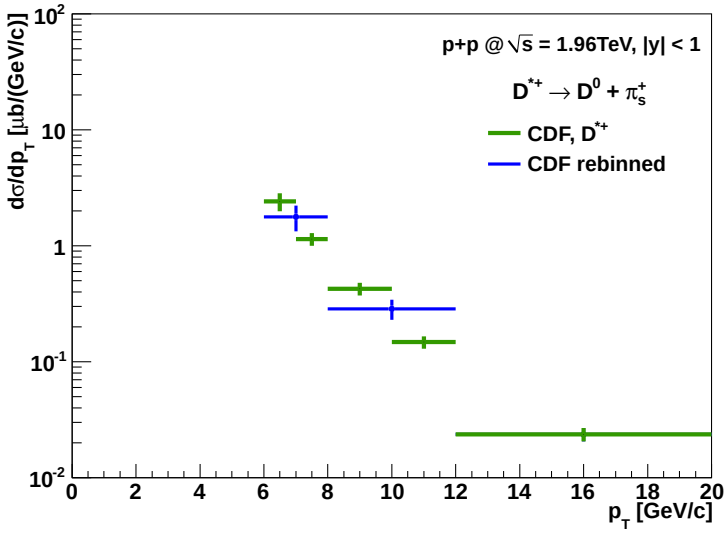

Figure 4.7: Rebinning of D^{*+} CDF data to ALICE bins.

There is an overlap between the ALICE bin at $5-6$GeV/c and the CDF bin for D^0 at $5.5-6$. However, as the overlap is incomplete, there is no meaningful comparison which can be made between those bins. Hence the bin between 5.5 and 6 GeV/c for the CDF data has been neglected. Additionally the ALICE results are for $p_T \leq 12$GeV/c, so the CDF bins above this threshold are not used for comparison. We end up with two CDF bins for each meson species, which can be compared directly to rescaled data.

4.3.2 Rapidity scaling

The CDF and ALICE detectors detect particles at different rapidity ranges - CDF measured D meson production within the region $|y| < 1.0$, whereas ALICE detects within the region $|y| < 0.5$. This means that there will be some extra scaling required, as the p_T spectra given by CDF and ALICE are in fact $\frac{d^2\sigma}{dydp_T}$ integrated with respect to y within the cutoff region. Usually in such scaling it is assumed that the ratio is approximately 2, but for higher precision the rapidity cutoffs were taken into account when making the pQCD predictions. However, it is still useful to examine how much scaling is performed when going between rapidity cutoffs. To determine the required scaling, the theoretical data from MNR for 1.96TeV at rapidity less than 0.5 was divided by the theoretical data for the same energy at rapidity less than 1. The result of this can be seen in figure 4.8, with the uncertainty band being defined by the maximum and minimum of this ratio caused by the alteration of the scales.
As can be seen, although there are statistical fluctuations in the spectrum due to varying the scales, especially at $p_T > 20$GeV/c, the ratio is always centred about 0.5. For the region we are looking at for the scaling, $p_T < 20$, the uncertainties are very small, being at most 15% from the centre.

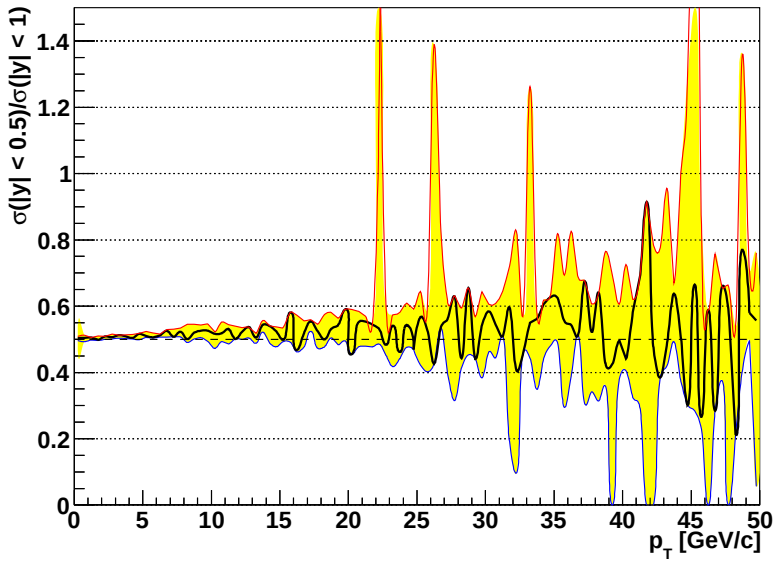

Figure 4.8: A demonstration of scaling between rapidities - here between $|y| < 0.5$ and $|y| < 1$.

4.3.3 Comparison between interpolation and rebinned data

Using the method described earlier in this section, the ALICE data was scaled to CDF energy, using MNR for D^{*+}, and both MNR and FONLL for D^0 and D^+. The results of these interpolations follow. The MNR calculations were performed by me on the cluster at the Physikalisches Institut at Heidelberg, whilst the scaling using FONLL was performed by Z. Conesa del Valle and obtained via private communication.

MNR interpolations

The interpolation from MNR for D^0 is shown in figure 4.9, for D^+ in figure 4.10, and for D^{*+} in figure 4.11. The yellow boxes represent the overall uncertainties on the interpolation ratio due to the variation of the scaling variables, using the scale set with the largest uncertainty contribution separately for each bin. The error bars on the actual points represent the experimental systematic errors. The interpolation was performed for each parameter set of the calculations separately, and the largest differences away from the central value were taken to be the error bars on the ratio. We can see here that there is a strong agreement between the ALICE data scaled down using this method and the CDF data, which is promising.

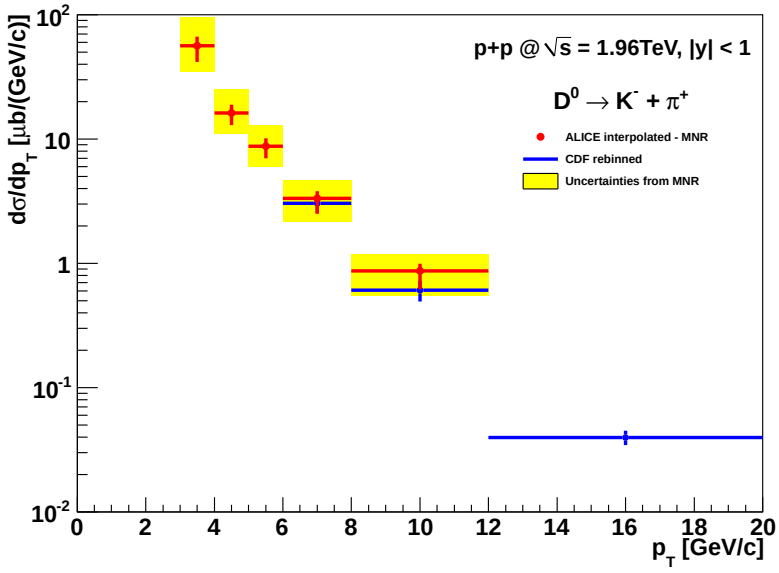

Figure 4.9: Interpolation to 1.96TeV using MNR for D^0.

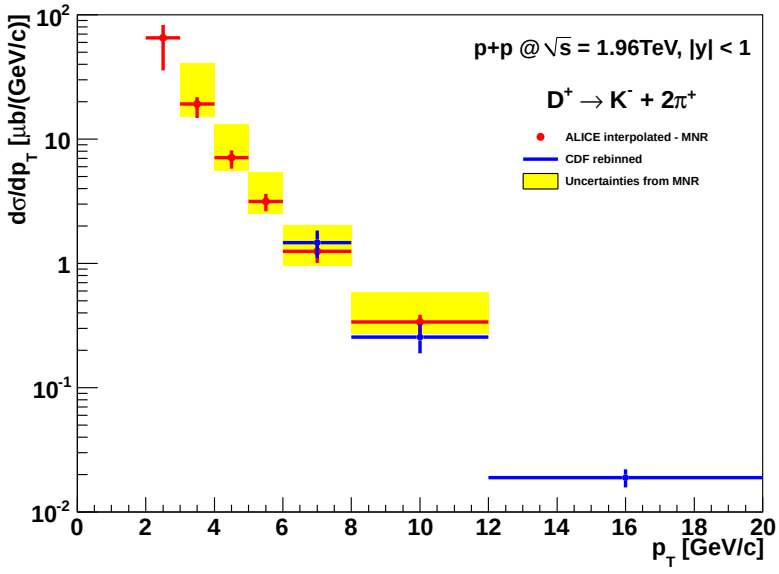

Figure 4.10: Interpolation to 1.96TeV using MNR for D^+.

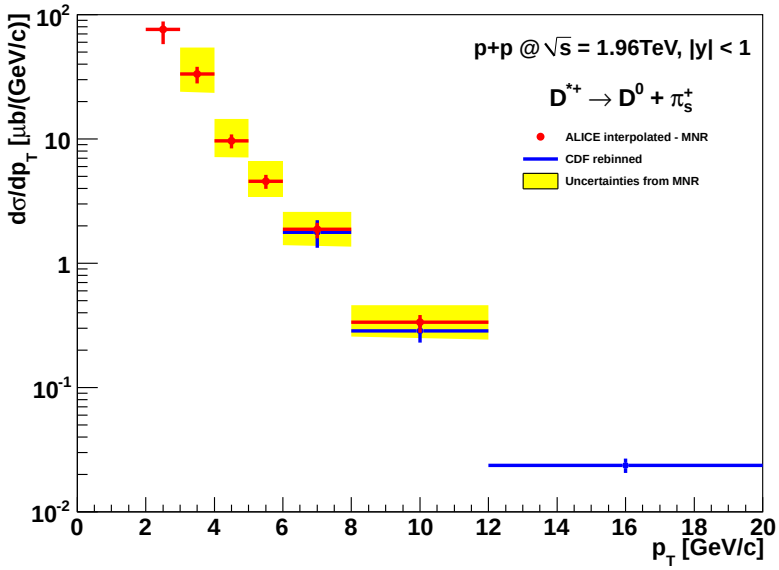

Figure 4.11: Interpolation to 1.96TeV using MNR for D^{*+}.

Comparison to FONLL

As previously mentioned, the FONLL calculation framework offers smaller uncertainties when altering the calculation parameters. Due to this, it is useful to compare the MNR interpolation with that achieved using the FONLL predictions. Figure 4.12 shows a comparison between the uncertainties of the MNR interpolation and the FONLL interpolation. As can be seen here, the MNR and FONLL interpolations agree with each other very strongly - crucially, however, the uncertainties on the FONLL interpolation are far smaller on the upper end. This implies that FONLL is a somewhat more accurate prediction to use for such exercises. As was discussed in section 3.4, this is expected as the MNR and FONLL frameworks are in essence identical - it is simply the resummation processes which vary, leading to FONLL's lower uncertainties.

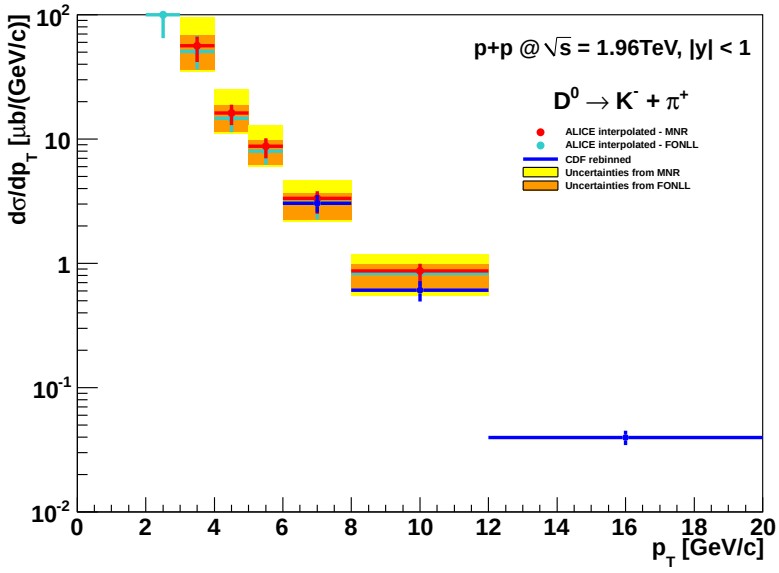

Figure 4.12: Comparison of the MNR and FONLL interpolations of D^0 to 1.96TeV.

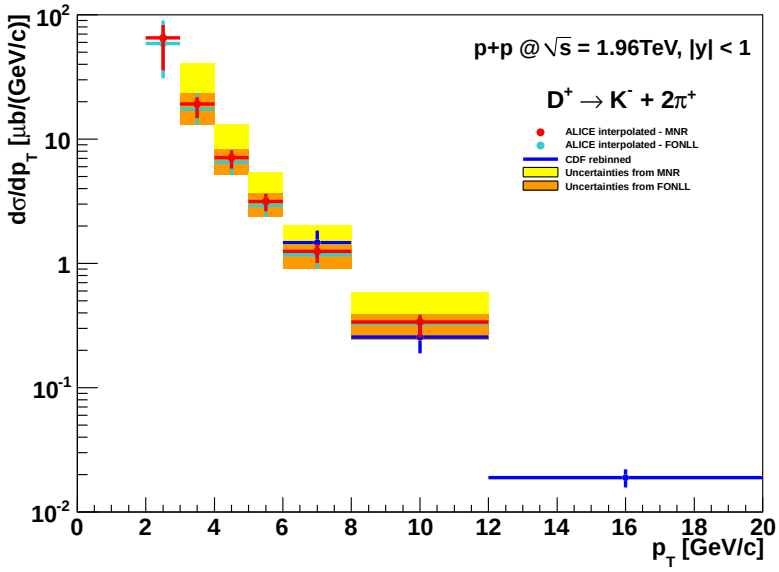

Figure 4.13: Comparison of the MNR and FONLL interpolations of D^+ to 1.96TeV.

Ratio of CDF to interpolated ALICE

To get a better idea of the reliability of the interpolations, ratios are taken between the interpolated data points and the CDF data points. This gives the percentage difference between the interpolation and the actual data points. Figures 4.14, 4.15 and 4.16 display these ratios for D^0 and D^{*+}, respectively.

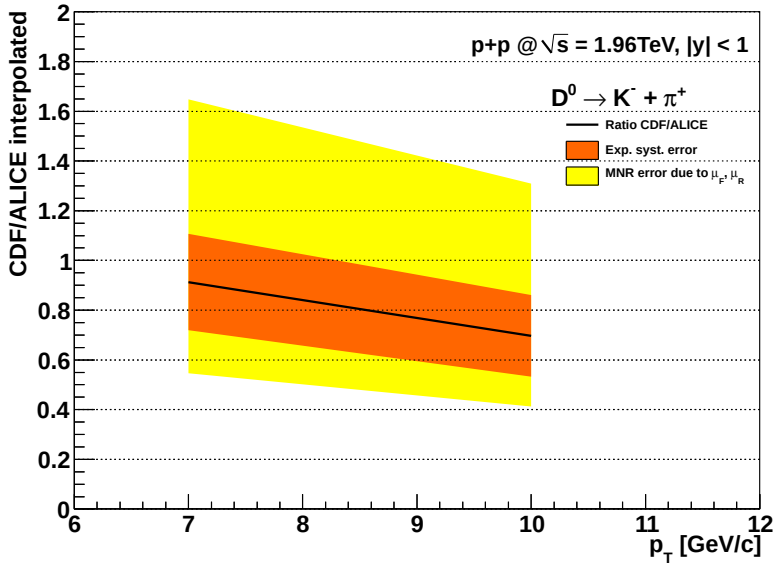

Figure 4.14: Ratio of MNR-interpolated data for D^0 to CDF data.

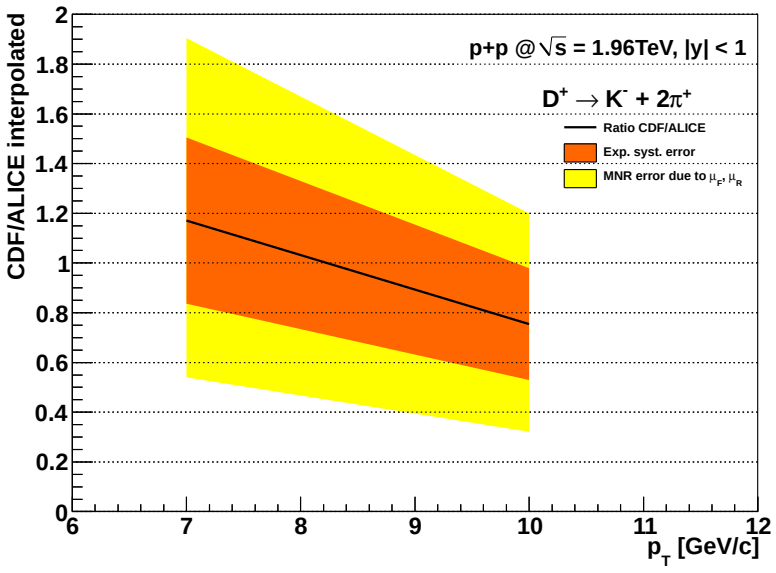

Figure 4.15: Ratio of MNR-interpolated data for D^+ to CDF data.

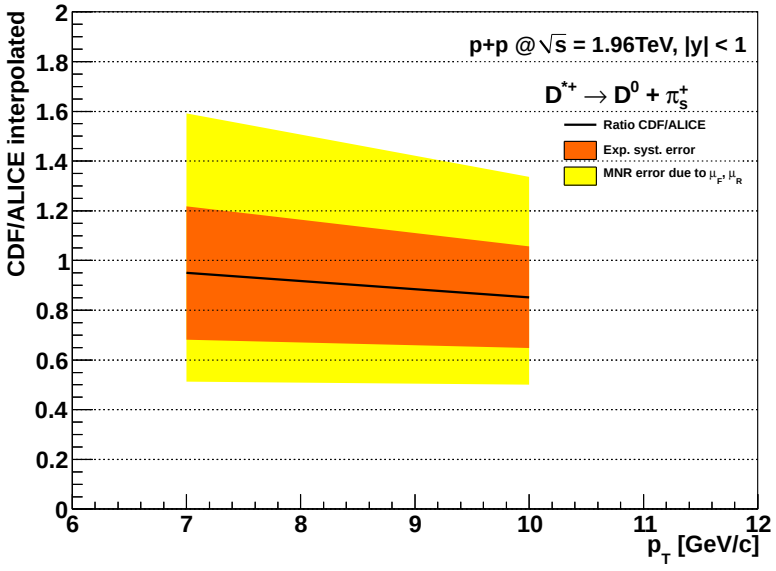

Figure 4.16: Ratio of MNR-interpolated data for D^{*+} to CDF data.

As the only p_T bins which match in range for both CDF and ALICE are those from 6-8 and from 8-12 GeV/c in both cases, it is only possible to use these two for such a direct comparison. We can see that for D^0 the interpolated data agrees with the CDF results within 10% for the first p_T bin, and within 30% for the bin at 10GeV/c. The uncertainties from the MNR calculations, however, are rather large - there is an upper uncertainty of about 80% from central for both p_T bins.
The agreement for D^{*+} is even stronger - here the lower p_T bin of the central interpolation agrees within 5%, and the upper within about 15%. This closer agreement is expected for the MNR calculations, as the predicted p_T spectrum from MNR mimics the fragmentation of charm quarks to D^{*+} mesons, assuming as an approximation that the fragmentation to other D mesons is identical. Again though, the uncertainties on the interpolation due to the scaling variables is large - as high as 70% on the upper end, and 50% on the lower end. Figures 4.17 shows the same ratios for D^0, this time including the uncertainties on the FONLL interpolation. We can see from this that the lower uncertainties on FONLL are about half as large as for MNR, and that the upper uncertainty is also slightly smaller for FONLL than for MNR.

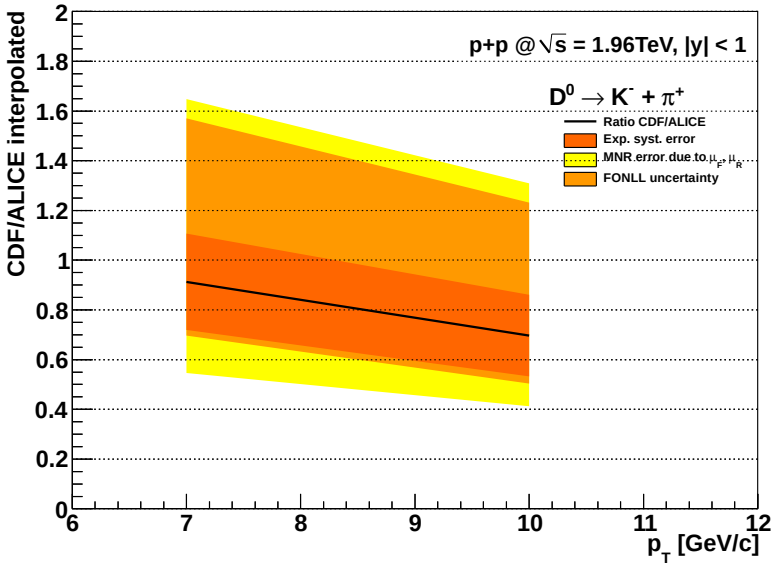

Figure 4.17: Ratio of MNR and FONLL interpolations for D^0 against CDF data.

Figure 4.18 shows this ratio also for D^+. Here the FONLL error envelope is roughly the same size as the MNR envelope, just shifted upwards slightly. We still see that

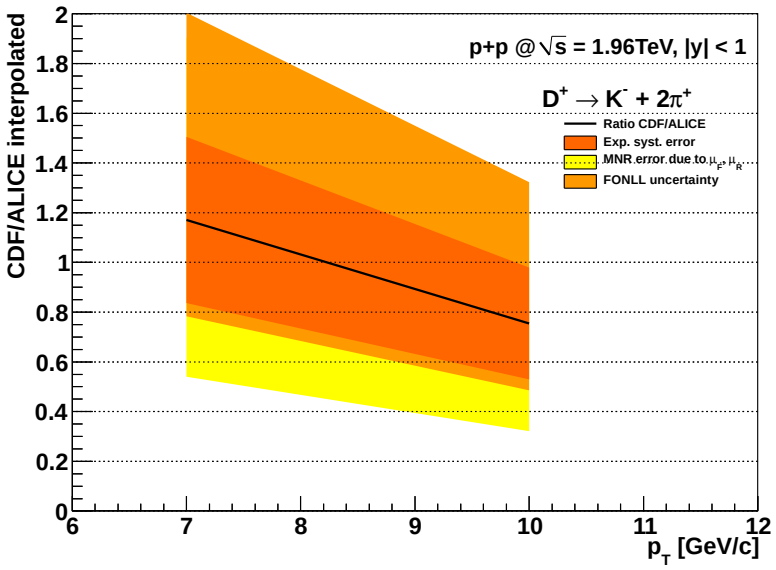

Figure 4.18: Ratio of MNR and FONLL interpolations for D^+ against CDF data.

the central line is within 20% of unity, which is a clear indicator that the scaling was successful.

4.3.4 Conclusions

Data from the proton-proton collisions at $\sqrt{s} = 7$TeV needs to be scaled down in order to make a reference for 2.76 TeV. To determine the validity of the method, a test was performed using available data from CDF. This was found to work well, with the deviation between this prediction and actual measurements at the second collision energy being small. Therefore the prediction for the 2.76TeV reference discussed in the next section will use this method. It has also been shown here that both MNR and FONLL are both valid calculation frameworks to use to interpolate data between different energies, with the two interpolation methods agreeing strongly with one another. Only the differences in uncertainties from the calculations distinguish the two frameworks from each other.

4.4 Interpolation to 2.76TeV

To create the reference spectrum, interpolation was performed via the same method as for the CDF data, and in this section the result of this will be outlined. Additionally, preliminary results from a short proton-proton run at $\sqrt{s} = 2.76$TeV were recently made available for D^0 and D^+, so the reference spectrum shall be compared also to the experimental data.

4.4.1 Comparisons

Figures 4.19, 4.20 and 4.21 display the ALICE data from 7TeV proton-proton collisions interpolated to 2.76TeV for D^0 and D^{*+}. Additionally, figures 4.22 and 4.23 show also the preliminary result from the ALICE experiment at 2.76 for D^0 and D^+, used as a cross check of the validity of the reference. To compare directly, the scaled data had to be rebinned, similarly to the CDF data previously, as the data at 2.76TeV was taken with a lower bin resolution than the data for 7TeV. As the data for D^{*+} at 2.76TeV is not yet preliminary, it has not been included here.
There is, as can be seen, a very strong agreement between the MNR and FONLL interpolations for all three meson species, again with only the overall uncertainties on the FONLL and MNR calculations distinguishing the two frameworks from one another. We see here also that there is a close agreement between the experimental data at the lower energy, and the scaled data.

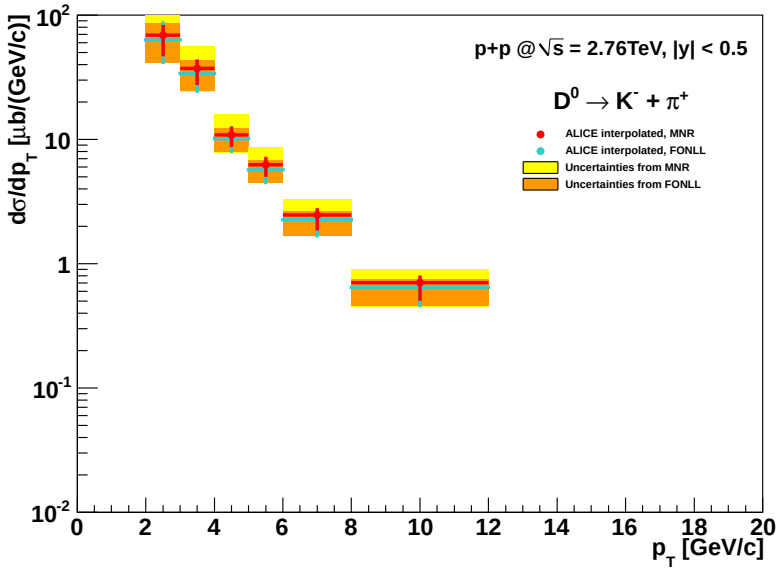

Figure 4.19: Interpolation of D^0 to 2.76TeV.

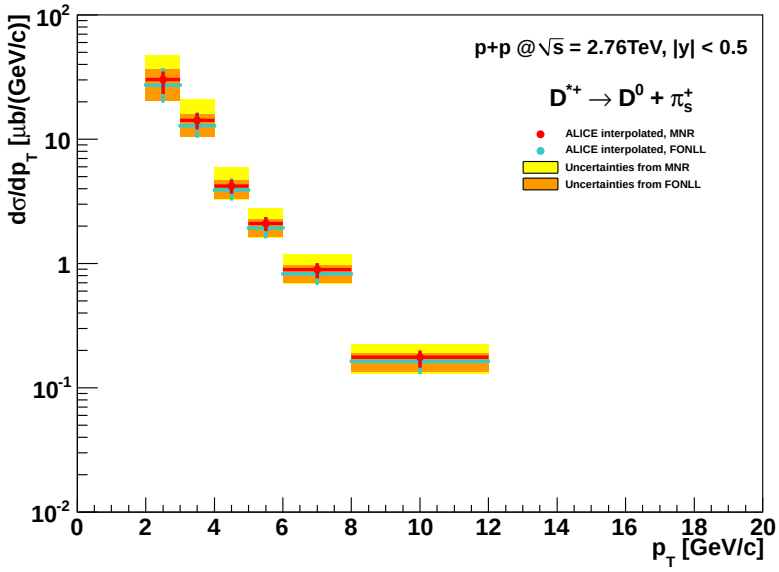

Figure 4.20: Interpolation of D^{*+} to 2.76TeV.

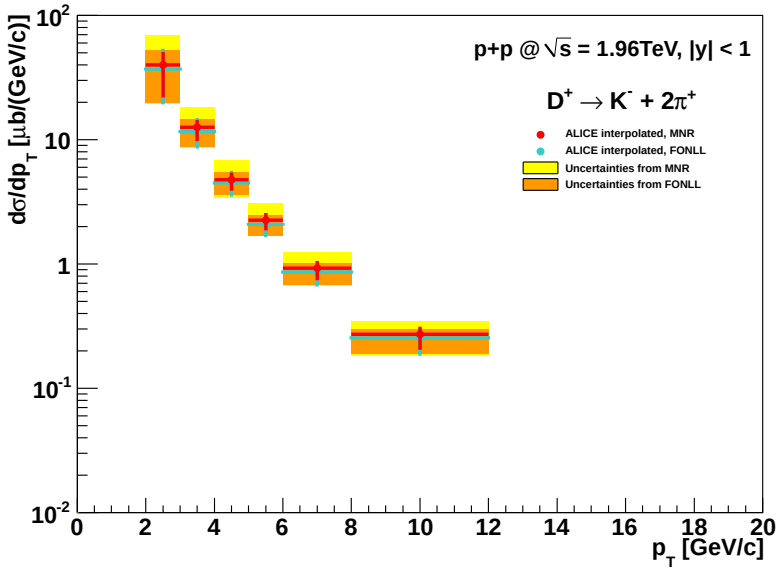

Figure 4.21: Interpolation of D^+ to 2.76TeV.

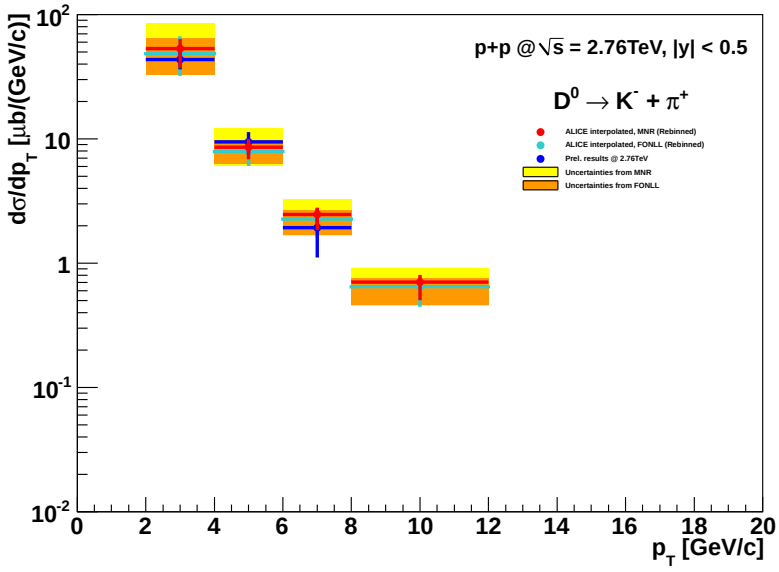

Figure 4.22: Interpolated data for D^0, compared with experimental data at 2.76TeV.

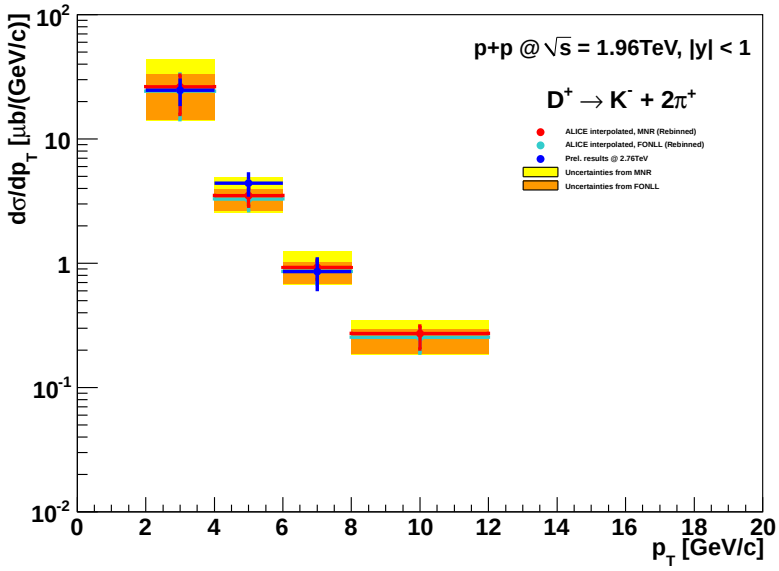

Figure 4.23: Interpolated data for D^+, compared with experimental data at 2.76TeV.

4.4.2 Conclusions

The high-statistics proton-proton experiment at 7TeV was successfully scaled down to 2.76TeV in order to provide a reference spectrum for PbPb collisions at this energy. The scaled reference was found to agree closely with the results of a short proton-proton run at this lower energy, confirming its validity as a reference. This reference will later be compared to the results of the PbPb collisions in order to determine the differences between interactions for the two collision schemes in high energy collisions.

5 Extracting the charm production cross section

Due to technical limitations and uncertainties it is not possible to measure the full cross section of particle production directly. The ALICE detector, for example, so far only measures D meson production between p_T = 2 and p_T = 12GeV/c in the experiment at 7TeV and between 2 and 8 for 2.76TeV, both with a rapidity cutoff of 0.5.[25] Thus, to achieve an estimate of the total cross section, it is necessary to extrapolate this data to full range. This section will discuss the method for this and the results, as well as an extraction of the total charm-anticharm cross section.

5.1 Method

The extrapolation was performed with the preliminary experimental spectra of D meson production after b-feeddown had been subtracted. The data used was, as with the interpolation, from D^0, D^{*+} and D^+, analysed via the decay channels outlined in section 3.5.
Firstly an integral was taken of the measured differential cross section - this integral is known as the visible cross section of D meson production. The visible cross sections contain corrections for their respective branching ratios. These visible cross sections give a measurement for the cross section of D meson production from charm fragmentation within the visible range.
To fill in the gaps in the regions where no data is taken, we rely on perturbative QCD calculations such as MNR and FONLL. We believe the general shape of the calculated differential cross sections in p_T and y to be correct, and use this to derive the extrapolation factor. The differential cross section spectra from the FONLL calculation framework were used in preference to MNR, due to the lower uncertainties and its separate calculations of fragmentation for each meson species.
To find the extrapolation factor, for each meson species, the spectrum for full rapidity was integrated over all p_T, and in the spectrum with the rapidity cutoff the prediction spectrum was integrated within the visible region. These two integrals were then divided by each other to give a factor by which the visible cross section could be multiplied to give an estimate of the full-range cross section for production of that meson species.
Once the cross sections of each individual meson species have been obtained, one can estimate the full cross section of charm-anticharm production, $\sigma_{c\bar{c}}$, by dividing the result by the meson's corresponding fragmentation ratio as outlined in section 3.2.
Each D-meson species was measured separately to provide an independent estimate of total charm production cross section, with varying systematic and statistical uncer-

tainties. Because of this, a method of combining the results is required. As D^0 and D^+ are discrete from each other, one can do this by adding the extrapolated meson cross sections and dividing by the sum of their fragmentation ratios. However as there is decay of D^* to D^0 one must add in this result differently - this is done by taking a weighted average between the cross section for charm-anticharm production derived from D^0 and D^+, with the equivalent cross section derived from D^{*+}. The weights used for this are $\frac{1}{\sigma^2_{\text{stat.}}}$. The final weighted average then represents an estimate of the full charm-anticharm cross section in the experiment.

5.2 Error propagation

The experimental data was taken within various p_T bins, each with its own statistical and systematic uncertainties. As the statistical uncertainties are uncorrelated from one another, it is possible to simply add the uncertainties in quadrature, taking into account the bin widths:

$$\sigma^2_{\text{stat}} = \sum_i (\sigma_{\text{stat}_i} \cdot \Delta p_{T_i})^2$$

However, the systematic uncertainties pose a different issue. The overall systematic uncertainty on each bin is the quadratic sum of both the uncertainty in cuts and the feed-down uncertainty as the two are uncorrelated with each other. However when comparing between bins, there is a correlation between the feed-down uncertainties, with no such correlation for the cut uncertainties. This means that the cut uncertainties must be added in quadrature between bins, whilst the feeddown uncertainties are added linearly:

$$\sigma^2_{\text{cuts}} = \sum_i (\sigma_{\text{stat}_i} \cdot \Delta p_{T_i})^2, \quad \sigma_{\text{feed}} = \sum_i (\sigma_{\text{feed}_i} \cdot \Delta p_{T_i}) \tag{5.1}$$

and then the final systematic uncertainty is the quadratic sum of these two results, with the upper and lower systematic uncertainty calculated separately.

$$\sigma^2_{\text{syst}} = \sigma^2_{\text{cuts}} + \sigma^2_{\text{feed}} \tag{5.2}$$

The experimental errors on the meson cross sections are extrapolated with the factor from the central FONLL predictions, as with the central results. The luminosity error on both the visible cross sections and the extrapolated meson cross sections are taken to be 7%,[26] and the branching ratio uncertainties are the percentage uncertainty on the branching ratio multiplied by the central value.

As well as the experimental uncertainties one must consider the uncertainties on the extrapolation factor itself. The FONLL calculations have uncertainties which stem from the alteration of the mass and the scaling variables μ_F and μ_R, as well as from the parton distribution function. To determine the extrapolation uncertainty, the ratios were taken separately for each parameter set. Then the changes in extrapolation factor from alteration of mass and scaling variables as outlined in table 3.1, as well as from the upper and lower estimates on PDF, are added in quadrature to give the final uncertainty on the factor.

$$\sigma^2_{\text{extr.}} = \sigma^2_{\text{extr}_{\text{mass}}} + \sigma^2_{\text{extr}_{\text{scales}}} + \sigma^2_{\text{extr}_{\text{PDF}}} \tag{5.3}$$

The extrapolation uncertainty is considered separately to all of the experimental uncertainties, with the upper and lower error bars being multiplied separately by the visible cross section to give the lower and upper extrapolation error on the meson productions cross sections.

To combine the uncertainties from D^0 and D^+ for the overall $c\bar{c}$ cross section, the uncertainties of each kind were added in quadrature before being divided by sum of the fragmentation ratios. Then to combine this with the overall $c\bar{c}$ cross section from D^{*+} with this, weighted averages of the uncertainties are taken using the same method as the central value, except the statistical uncertainty which is propagated as:

$$\frac{1}{\sigma^2_{\text{stat}}} = \left(\frac{1}{\sigma^{D^0D^+}_{\text{stat}}}\right)^2 + \left(\frac{1}{\sigma^{D^{*+}}_{\text{stat}}}\right)^2 \tag{5.4}$$

5.3 Results for 2.76TeV

The visible cross sections derived from the preliminary results of the proton-proton run at 2.76TeV are shown in (5.5):

$$\begin{aligned}\sigma^{vis}(D^0) &= 73 \pm 10(\text{stat.})^{+23}_{-26}(\text{syst.}) \pm 5(\text{lum.}) \pm 1(\text{br.})\mu\text{b} \\ \sigma^{vis}(D^+) &= 60 \pm 13(\text{stat.})^{+15}_{-19}(\text{syst.}) \pm 4(\text{lum.}) \pm 1(\text{br.})\mu\text{b}\end{aligned} \tag{5.5}$$

These were extrapolated to full phase space using the ratios given in appendix B, and the results are shown in (5.6):

$$\begin{aligned}\sigma^{tot}_{c\bar{c}}(D^0) &= 1.49 \pm 0.20(\text{stat.})^{+0.47}_{-0.53}(\text{syst.}) \pm 0.10(\text{lum.}) \pm 0.02(br.)^{+0.65}_{-0.15}(\text{extr.})\text{mb} \\ \sigma^{tot}_{c\bar{c}}(D^+) &= 1.21 \pm 0.25(\text{stat.})^{+0.31}_{-0.39}(\text{syst.}) \pm 0.08(\text{lum.}) \pm 0.03(br.)^{+0.55}_{-0.11}(\text{extr.})\text{mb}\end{aligned} \tag{5.6}$$

Finally, the open charm cross section for 2.76TeV is shown in (5.7).

$$\sigma^{tot}_{c\bar{c}}(\text{ALICE}, 2.76\text{TeV}) = 3.45 \pm 0.41(\text{stat.})^{+0.72}_{-0.84}(\text{syst.}) \pm 0.17(\text{lum.})^{+1.09}_{-0.24}(\text{extr.})\text{mb} \tag{5.7}$$

The largest source of uncertainty here is the systematic error – this is because only a relatively short run was performed at 2.76TeV, causing the result to be based on a smaller amount of data than usual. The overall error bar (taken as a quadratic sum of all uncertainties) is $^{+40}_{-28}\%$

5.4 Results for 7TeV

The visible cross sections for D meson production in pp collisions at 7TeV are given in (5.8).

$$\begin{aligned}
\sigma^{vis}(D^0) &= 206 \pm 20(\text{stat.})^{+25}_{-48}(\text{syst.}) \pm 14(\text{lum.}) \pm 3(\text{br.})\mu\text{b} \\
\sigma^{vis}(D^{*+}) &= 96 \pm 14(\text{stat.})^{+9}_{-14}(\text{syst.}) \pm 7(\text{lum.}) \pm 1(\text{br.})\mu\text{b} \\
\sigma^{vis}(D^+) &= 113 \pm 17(\text{stat.})^{+19}_{-37}(\text{syst.}) \pm 8(\text{lum.}) \pm 3(\text{br.})\mu\text{b}
\end{aligned} \tag{5.8}$$

The extrapolation ratios for 7TeV, and their uncertainties, from the FONLL calculations are outlined in appendix C. The extrapolation factor was also determined using the MNR framework as a cross-check and was found to agree with the FONLL calculation; this is also shown in appendix C.
The total production cross sections derived from these extrapolations is given in (5.9).

$$\begin{aligned}
\sigma^{tot}_{c\bar{c}}(D^0) &= 4.02 \pm 0.38(\text{stat.})^{+0.49}_{-0.93}(\text{syst.}) \pm 0.28(\text{lum.}) \pm 0.05(br.)^{+1.17}_{-0.61}(\text{extr.})\text{mb} \\
\sigma^{tot}_{c\bar{c}}(D^{*+}) &= 1.71 \pm 0.25(\text{stat.})^{+0.16}_{-0.26}(\text{syst.}) \pm 0.12(\text{lum.}) \pm 0.03(br.)^{+0.57}_{-0.20}(\text{extr.})\text{mb} \\
\sigma^{tot}_{c\bar{c}}(D^+) &= 2.18 \pm 0.32(\text{stat.})^{+0.36}_{-0.71}(\text{syst.}) \pm 0.15(\text{lum.}) \pm 0.05(br.)^{+0.66}_{-0.31}(\text{extr.})\text{mb}
\end{aligned} \tag{5.9}$$

Finally, the resulting open charm cross sections at 7TeV is shown in (5.10).

$$\sigma^{tot}_{c\bar{c}}(\text{ALICE}, 7\text{TeV}) = 7.73 \pm 0.54(\text{stat.})^{+0.74}_{-1.38}(\text{syst.}) \pm 0.43(\text{lum.})^{+1.90}_{-0.87}(\text{extr.})\text{mb} \tag{5.10}$$

For the collisions at $\sqrt{s} = 7$TeV, the experimental data was taken over a longer period of time, reducing the systematic and statistical uncertainties. This means that here, the extrapolation uncertainty is the largest contributor to the overall uncertainty. The overall uncertainty is $^{+28}_{-23}\%$, meaning a smaller uncertainty band than that for the experiment at 2.76TeV. This has been accepted as ALICE's preliminary result for this measurement.
As is seen in the tables in appendices B and C, due to the small phase space only about 5% of the total cross section was typically measured – this is implied by the size of

the extrapolation factor. Also displayed in the appendices are the individual contributions to the extrapolation factor from the p_T and y spectra. We see that the factor for p_T extrapolation is approximately 2 at 7TeV, and approximately 3 at 2.76TeV. This difference can be explained kinematically as the lower energy shifts the experimental spectrum closer to $p_T = 0$ – due to this shift we measure less of the total cross section in the visible phase space region. In terms of the rapidity contribution, the factor for 7TeV is approximately 8.5, and for 2.76 TeV it is 7.3. Similarly to p_T, the lower collision energy favours lower rapidity, and so as the ALICE measurement centres around zero rapidity, a higher proportion of the produced particles are measured within this rapidity coverage at the lower energy.
Another interesting point of note is that the contribution from the rapidity spectrum is not dependent on the meson species considered, whereas the p_T contribution varies between the different meson types. This implies that the rapidity spectrum has no dependence on the mass of the light quark with which the charm quark fragments, whilst there is a difference in the p_T spectrum caused by the fragmentation process.
The total cross sections can be used also to calculate P_v, which is a measurement of the fraction of D mesons produced in a vector state. It is defined in equation 5.11 as the ratio between the D^{*+} production cross section against the sum of the cross sections of D^{*+} and D^+ production, once the fraction of the cross section contributed by D^{*+} decay has been removed.

$$P_v = \frac{\sigma_{c\bar{c}}^{tot}(D^{*+})}{\sigma_{c\bar{c}}^{tot}(D^+) + \sigma_{c\bar{c}}^{tot}(D^{*+}) \cdot \mathscr{B}_{D^{*+}\to D^0\pi^+}} \tag{5.11}$$

In the branching ratio, we took the proportion of D^{*+} not decaying to D^+, i.e. the proportion which decays to D^0.
For the ALICE measurement this was found to be

$$P_v = 0.51 \pm 0.09(\text{stat.})^{+0.08}_{-0.14}(\text{syst.}) \pm 0.01(\text{br.})^{+0.21}_{-0.08}(\text{extr.}) \tag{5.12}$$

which is lower than what would be expected from simple spin counting, which would result in P_v equal to 0.75 as there are three spin states for D^{*+} and only one for D^+. This measurement agrees within error bars with LEP (5.13), and with ATLAS' measurement (5.14).

$$P_v(\text{LEP}) = 0.62 \pm 0.02(\text{stat.} \oplus \text{syst.}) \pm 0.02(\text{br.}) \tag{5.13}$$

$$P_v(\text{ATLAS}) = 0.63 \pm 0.03(\text{stat.})^{+0.02}_{-0.03}(\text{syst.}) \pm 0.02(\text{br.})^{+0.04}_{-0.02}(\text{extr.}) \tag{5.14}$$

5.5 Comparison to ATLAS and LHCb

ATLAS[27] and LHCb,[28] two other experiments at the LHC, have also made measurements for charm-anticharm production cross sections at 7TeV.
The ATLAS detector measured for $p_T \geq 3.5$GeV/c, and to a pseudorapidity $|\eta| \leq 2.1$. Pseudorapidity is a measurement almost equivalent to rapidity, substituting the overall magnitude of momentum instead of energy into equation 3.4. This means that ATLAS had a greater rapidity coverage, but measured over a smaller range of transversal momentum. Their extrapolation used the POWHEG-PYTHIA[22] calculation framework. LHCb, on the other hand, measured in the region $0 \leq p_T \leq 8$GeV/c, and $2 \leq y \leq 4.5$ and extrapolated using PYTHIA.
The result of the ATLAS extrapolation is shown in (5.15), and LHCb in (5.16).

$$\sigma_{c\bar{c}}^{tot}(\text{ATLAS}) = 7.13 \pm 0.28(\text{stat.})^{+0.90}_{-0.66}(\text{syst.}) \pm 0.78(\text{lum.})^{+3.82}_{-1.90}(\text{extr.})\text{mb} \tag{5.15}$$

As has previously been seen, the shape of the rapidity spectrum is far more regular than that of the p_T spectrum, especially at lower p_T. Due to this, the extrapolation uncertainty of ATLAS' extrapolation is larger than that for ALICE, as whilst the ALICE data measured approximately half of the full p_T spectrum within its range, ATLAS only measured about a seventh. This means that although the actual experimental uncertainties from ATLAS are smaller than those from ALICE, their higher extrapolation errors give overall a greater uncertainty band of about $^{+56}_{-31}$%.

$$\sigma_{c\bar{c}}^{tot}(\text{LHCb}) = 6.10 \pm 0.93(\text{overall})\text{mb} \tag{5.16}$$

The uncertainty quoted is the overall uncertainty as published by LHCb. As the LHCb measurements were made for $p_T \leq 8$, where the vast majority of the yield lies, their extrapolation uncertainties were far smaller than for ALICE.

5.6 Plot of cross section against centre-of-mass energy

Figure 5.1 is a plot of the total charm-anticharm cross section published by other experiments,[11, 27–30] as well as the ALICE result outlined in section 5.4, against the centre of mass energy. The black curves are the next-to-leading-order predictions from the MNR calculation framework and its uncertainties. The error boxes around the ATLAS and ALICE points denote the extrapolation uncertainties alone, whilst the error bars are the overall uncertainties obtained by adding all uncertainties in quadrature.

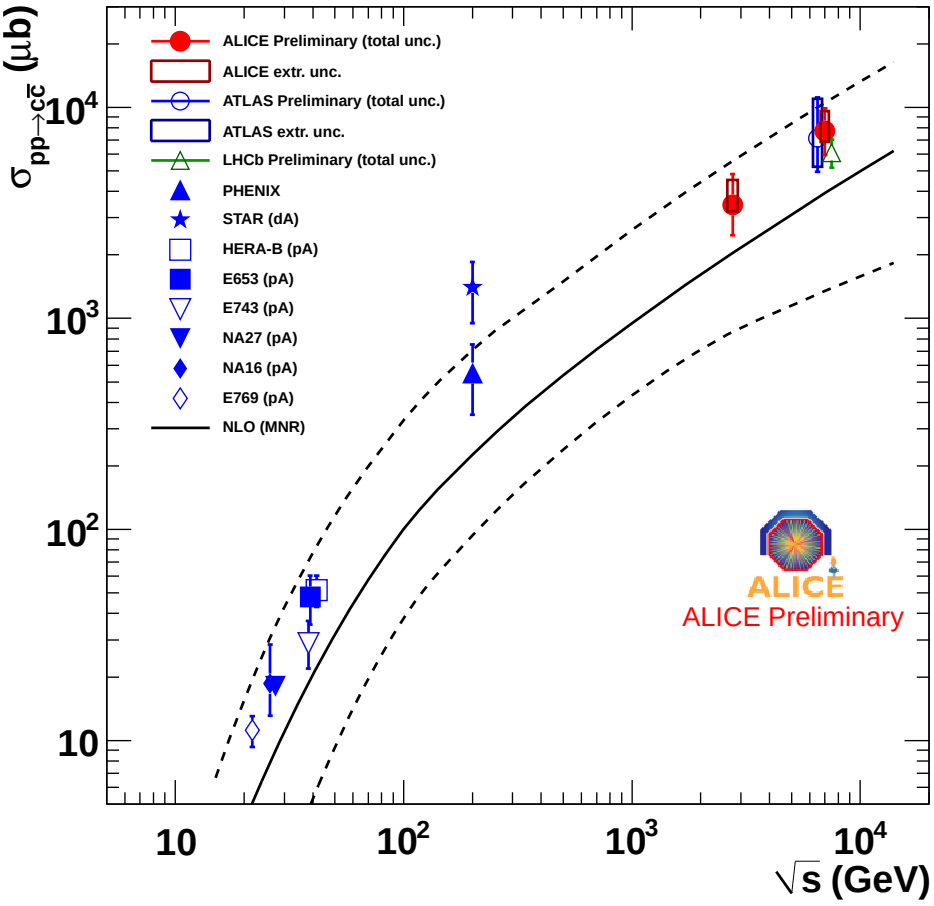

Figure 5.1: Plot of open charm cross section as a function of $\sqrt{s}$, including extrapolations from ATLAS and LHCb.

We can see here that there is great agreement between ALICE, LHCb and ATLAS, despite covering three different ranges in phase space, even taking into account that the extrapolation errors are somewhat correlated. Due to this agreement, the points at 7TeV had to be offset very slightly to allow them to be compared more easily.
It can also be seen from the collision energy dependence that all the data points are described by the upper band of the NLO calculations, apart from the STAR result from RHIC. This is a very promising result.
This plot has been accepted as preliminary by the ALICE collaboration and has been presented at two recent international conferences: Quark Matter 2011 in Annecy, France,[31] and Hadron 2011 in München, Germany.[32]

5.7 Conclusions

The measured cross sections of D meson production from the ALICE detecter were successfully extrapolated to full phase space, allowing an extraction of the overall charm-anticharm production cross section. This was found to be $7.73^{+2.15}_{-1.77}$mb, which is in strong agreement with both ATLAS and LHCb, as well as with the theoretical trend from next-to-leading-order calculations.
The described extrapolation method has been committed as a macro to the repository for the AliROOT package, an alternative version of ROOT specific to ALICE data analysis.
The structure of the code is such that it can easily be edited to incorporate different collision schemes, energies or decay channels, so long as the correct input files are available. In light of this, over the next month I shall be extending this method to the analysis of electron spectra from heavy flavour production detected by ALICE.

6 Conclusion and Outlook

This project centred on the analysis and extrapolation of charmed meson cross sections. Perturbative QCD calculations were performed using the MNR framework at various energies and with various parameters to simulate the production of charm and bottom quarks as a result of proton-proton collisions. The calculations for beauty were compared to both experimental and theoretical data published by the CMS experiment, and found to be in strong agreement with these.

The calculations for charm were then used to scale differential cross sections measured at a collision energy of 7TeV down to 2.76TeV, in order to provide a reference spectrum against which data from lead-lead collisions can later be compared. Prior to this a test of the method was performed using already-available data from the CDF experiment at Fermilab, to ensure that the scaled spectra would be correct. MNR calculations, when used to scale the experimental data for D^0, D^+ and D^{*+} from ALICE, were found to create a reference which agreed well with the data measured by CDF, and the interpolation using FONLL was also very successful, with even smaller error bars than MNR. The reference spectra for 2.76TeV were then created using this method. In the case of D^0 and D^+, it was also possible to directly compare this reference with low-statistics proton-proton data recently taken at this collision energy, and again there was good agreement between the scaled data and experimental results.

The cross sections for D meson production were then extrapolated to full phase space using the FONLL calculations, allowing technical limitations in the measurements to be negated in order to gain estimate of the total cross section of meson production. From this it was then possible to extract the full charm-anticharm production cross section, which was found to agree with measurements of the same quantity by both LHCb and ATLAS, as well as with the theoretical trend predicted by next-to-leading-order pQCD calculations. The result of this extrapolation was accepted as the ALICE preliminary result.

The method used for the extrapolation will next be used to analyse the leptonic decays of heavy quark matter, in order to give even further insight into the nature of the QGP medium.

Appendices

A CDF data and rebinning

These tables display the differential cross sections measured by the CDF collaboration[24] based at the Tevatron at Fermilab, as well as the data rebinned to the ALICE bins for better comparison when data was scaled.

p_T range	Central p_T	$d\sigma(\|y\| \leq 1)/dp_T$ [nb/GeV/c]		
GeV/c	GeV/c	D^0	D^{*+}	D^+
$5.5-6$	5.75	$7837 \pm 220 \pm 884$	–	–
$6-7$	6.5	$4056 \pm 93 \pm 441$	$2421 \pm 108 \pm 424$	$1961 \pm 69 \pm 332$
$7-8$	7.5	$2052 \pm 58 \pm 227$	$1147 \pm 48 \pm 145$	$986 \pm 28 \pm 156$
$8-10$	9.0	$890 \pm 25 \pm 107$	$427 \pm 16 \pm 54$	$375 \pm 9 \pm 62$
$10-12$	11.0	$327 \pm 15 \pm 41$	$148 \pm 8 \pm 18$	$136 \pm 4 \pm 24$
$12-20$	16.0	$39.9 \pm 2.3 \pm 5.3$	$23.8 \pm 1.3 \pm 3.2$	$19.0 \pm 0.6 \pm 3.2$

Table A.1: Measured differential cross sectons of D mesons at 1.96TeV from CDF.[24]

p_T range	Central p_T	$d\sigma(\|y\| \leq 1)/dp_T$ [nb/GeV/c]		
GeV/c	GeV/c	D^0	D^{*+}	D^+
$6-8$	7.0	$3054 \pm 75.5 \pm 334$	$1784 \pm 78 \pm 285$	$1474 \pm 49 \pm 244$
$8-12$	10.0	$609 \pm 20 \pm 74$	$288 \pm 12 \pm 36$	$256 \pm 8 \pm 43$

Table A.2: CDF data rebinned to ALICE p_T bins.

B Extrapolation factors for 2.76TeV

These are the factors used for extrapolating the D meson production cross sections at 2.76TeV to full phase space, from the FONLL calculations, as well as a full breakdown of the uncertainties involved. Also noted are the contributions to the central extrapolation factor from the p_T and y spectra; these are not contributions to the uncertainty.

D^0 central:	20.502	
Contributions	p_T: 2.807	y: 7.304
Scales:	+8.970	-1.821
Mass:	+0.240	-0.827
Overall:	+8.973	-2.000

Table B.1: Extrapolation ratios and uncertainties for D^0 at 2.76TeV

D^+ central:	20.237	
Contributions	p_T: 2.771	y: 7.304
Scales:	+9.113	-1.763
Mass:	+0.082	-0.707
Overall:	+9.113	-1.899

Table B.2: Extrapolation ratios and uncertainties for D^+ at 2.76TeV

C Extrapolation factors for 7TeV

The following are the extrapolation factors used to extrapolate to full phase space at 7TeV, as in Appendix B. Also shown here is the extrapolation ratio calculated from the MNR spectra, which was used as a cross check for the FONLL extrapolation factor.

D^0 central:	19.507	
Contributions	p_T: 2.280	y: 8.557
Scales:	+5.600	-2.719
Mass:	+0.109	-0.618
PDF:	+0.780	-1.03
Overall:	+5.655	-2.973

Table C.1: Extrapolation ratios and uncertainties for D^0 at 7TeV

D^{*+} central:	17.919	
Contributions	p_T: 2.094	y: 8.557
Scales:	+5.915	-1.798
Mass:	+0.123	-0.540
PDF:	+0.655	-0.874
Overall:	+5.953	-2.071

Table C.2: Extrapolation ratios and uncertainties for D^{*+} at 7TeV

D^+ central:	19.314	
Contributions	p_T: 2.257	y: 8.557
Scales:	+5.780	-2.494
Mass:	+0.000	-0.527
PDF:	+0.753	-0.999
Overall:	+5.828	-2.738

Table C.3: Extrapolation ratios and uncertainties for D^+ at 7TeV

D^+ central:	20.716	
Contributions	p_T: 2.422	y: 8.552
Scales:	+4.808	-1.450
Mass:	+2.004	-1.702
Overall:	+5.209	-2.236

Table C.4: Extrapolation ratios and uncertainties at 7TeV from MNR.

References

[1] B. Alessandro *et al.* (ALICE collab.), ALICE Performance Report, Volume II, J.-Phys. G: Nucl. Part. Phys. 32: 1295 (2006).

[2] P. Braun-Munzinger, J. Stachel, Nature 448: 302 (2007).

[3] CERN website, http://www.cern.ch.

[4] M. Mangano, P. Nason, G. Ridolfi; Nuclear Physics B 373: 295 (1992).

[5] M. Cacciari *et al.*, JHEP 0809: 127 (2008).

[6] J. Pumplin *et al.* (CTEQ collab.), JHEP0207:012 (2002).

[7] J. Gasser, H. Leutwyler, Phys. Rept. 87: 77 (1982).

[8] HERA-LHC Workshop Proceedings: Summary report of Working Group 3 (arXiv:hep-ph/0601164v2) (2007).

[9] J.C. Collins, Phys. Rev. D58: 094002 (1998).

[10] C. Peterson *et al.*, Phys. Rev. D27: 105 (1983).

[11] C. Lourenço, H.K. Wöhri, Phys. Rept. 433: 127 (2006) .

[12] S. Schael *et al.* (ALEPH collab.), Phys. Rept. 427: 257 (2006).

[13] V. G. Kartvelishvili, A. K. Likhoded, and V. A. Petrov, Phys. Lett. B78, 615 (1978).

[14] M. G. Bowler, Zeit. Phys. C11: 169 (1981).

[15] P. D. B. Collins and T. P. Spiller, J. Phys. G11: 1289 (1985).

[16] The Les Houches Accord PDF Interface, http://projects.hepforge.org/lhapdf.

[17] M. Cacciari, M. Greco, P. Nason, JHEP 05: 007 (1998).

[18] L. Gladilin, arXiv:hep-ex/9912064 (1999).

[19] K. Ackerstaff *et al.* (OPAL collab.), Eur. Phys. J. C1: 439 (1997).

[20] K. Nakamura *et al.* (Particle Data Group), Journal of Physics G 37: 075021 (2010).

[21] The CMS Collaboration, Phys. Rev. Lett. 106:112001 (2011).

[22] T. Sjöstrand, S. Mrenna, P. Skands, "PYTHIA6.4 Physics and Manual," JHEP 0605:026 (2006).

[23] S. Frixione, B.R. Webber, JHEP06: 029 (2002).

[24] D. Acosta *et al.* (CDF collab.), Phys. Rev. Lett. 91:241804 (2003).

[25] Y. Wang, University of Heidelberg, Ph.D. thesis (in preparation).

[26] K. Oyama *et al.* (ALICE Collaboration), proc. of the XXII Quark Matter Conference (eds. Yves Schutz and Urs Widemann), Annecy, France (2011); to be published in J. Phys. G: Nucl. Part. Phys.

[27] ATLAS collaboration, internal note: ATLAS-CONF-2011-017 (2011).

[28] LHCb collaboration, internal note: LHCb-CONF-2010-013 (2010).

[29] J. Adams *et al.* (STAR collab.), Phys. Rev. Lett. 94: 62301 (2005).

[30] A. Adare *et al.* (PHENIX collab.), arXiv:1005.1627v2 (2010).

[31] Quark Matter 2011: XXII International Conference on Ultrarelativistic Nucleus-Nucleus Collisions, Annecy, France (2011).

[32] XIV International Conference on Hadron Spectroscopy, München, Germany (2011).

Acknowledgements

Many thanks go to my supervisor Dr. Kai Schweda, who was also my seminar tutor for the particle physics course (Experimentalphysik 5) here at the University of Heidelberg. The opportunity to work with data from the ALICE experiment on such a fascinating project has been invaluable to me. His constant assistance and guidance in all the work I have done, as well as his enthusiasm throughout, have been a major driving force throughout this year.
Thanks also to Prof. Dr. Johanna Stachel, the lecturer for the particle physics course, whose teaching was incredibly useful in understanding many of the concepts drawn upon in this project.
Thanks go to Dr. Andrea Dainese, and the rest of the PWG3 group, for allowing me to present my methods and findings in the D2H (paper preparation) meetings throughout the year – the experience of presenting in these meetings is something that will stay with me for a long time, and the comments and suggestions made by the group throughout were incredibly useful. I'm incredibly grateful also to the Physics Forum of the ALICE project for allowing me to present my findings to them, and accepting my work as a preliminary result for the collaboration. That my work was viewed with such significance was an immeasurable boost to me, allowing me to remain motivated throughout, no matter how heavy the workload became at times.
I'd like to thank also Dr. Zaida Conesa del Valle, who provided most of the experimental data throughout and was always quick to clarify matters when new versions of data were made available, or when the binning or scaling of the data was unclear. Thanks also to Yifei Wang and Dr. Renu Bala for their help with data.
I'd like also to thank the creators of the FeynMF package for LaTeX, which was used to create the Feynman diagrams displayed in this report.
Finally I would like to express my gratitude also to Martin Gabel for his assistance with technical details when using the cluster; to Dr. Matteo Cacciari for providing the PDF error band on the NLO calculations used in figure 5.1; to Robert Grajcarek who provided much aid and support in terms of learning how to use ROOT; and to Dominik Neuenfeld who provided much advice on interfacing with the MNR program.
This work has been supported by the Helmholtz Association under contract number VH NG-147 and and the Federal Ministry of Education and Research under promotional reference 06HD197D.